ORIGINAL ARTICLE

lajss.org© Latin American Journal of Solids and Structures

www.lajss.org

Study of propellant sloshing with passive mitigation in the stability of a micro- launch vehicle

Domingos Sávio Aguiar[a*], Carlos d'Andrade Souto[a], Maurício Guimaraes da Silva[a], Guilherme da Silveira[a]

[a]Instituto de Aeronáutica e Espaço – IAE, São José dos Campos, SP, Brasil. E-mails: domingosdsa@fab.mil.br, soutocds@fab.mil.br, guimaraesmgs1@fab.mil.br, guilhermegs1@fab.mil.br

* Corresponding author

https://doi.org/10.1590/1679-7825/e8427

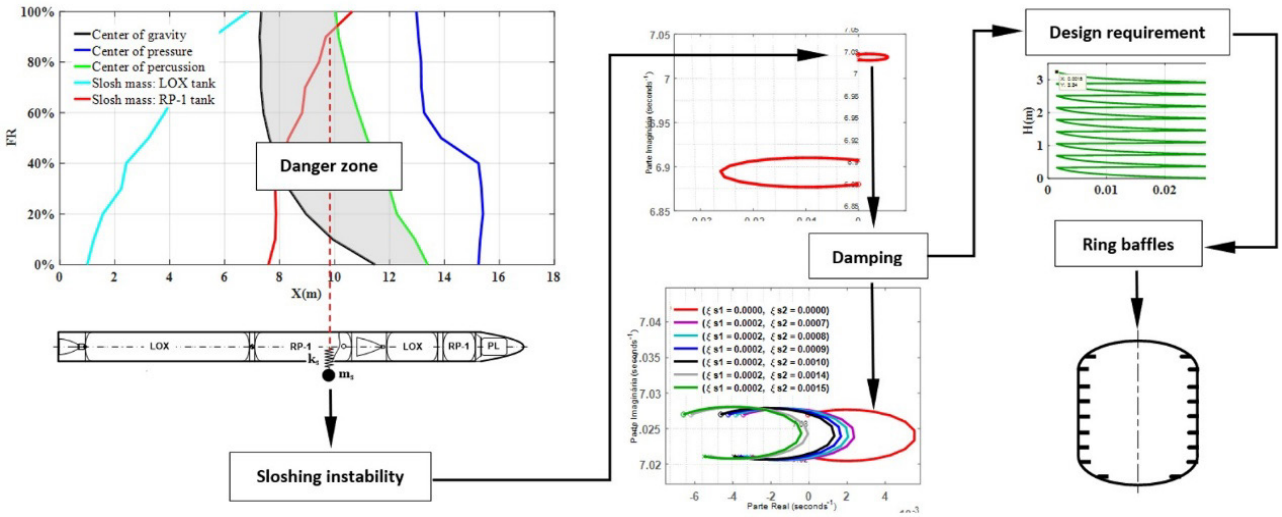
Abstract

This work presents stability analyzes results for a micro-launch vehicle (Micro-LV) considering the effects of sloshing. A conceptual Two-Stage to Orbit (TSTO) Micro-LV utilizing liquid propulsion with LOX and RP-1 is developed. Its mission objective is to deploy a payload of 100 kg into low Earth orbit (LEO) at an altitude of 300 km. Linearized equations of motion for rigid and flexible bodies, along with engine inertia effects and sloshing, are considered and arranged in a state-space formulation. Transfer functions relating the pitch angle $\emptyset_y$ and the engine gimbal angle, β_{Ey} are determined for open-loop stability analyses considering a proportional-derivative (PD) attitude controller. It is observed that at a FR of 90%, the RP-1 tank exhibits instability because its sloshing mass is situated between the center of percussion (CP) and the center of gravity (CG) of the Micro-LV, in the area referred as the danger zone. A solution for the passive mitigation of sloshing instability is implemented by introducing ring baffles with a minimum damping requirement of 0.15%, and its effect on the vehicle's stability is analyzed.

Keywords

Micro-LV, sloshing, danger zone, stability, damping, ring baffles.

Graphical Abstract



Received December 8, 2024. In revised form February 11, 2025. Accepted March 4, 2025. Available online March 6, 2025.
https://doi.org/10.1590/1679-7825/e8427

Latin American Journal of Solids and Structures. ISSN 1679-7825. Copyright © 2025. This is an Open Access article distributed under the terms of the Creative Commons Attribution License, which permits unrestricted use, distribution, and reproduction in any medium, provided the original work is properly cited.

1 INTRODUCTION

According to Wekerle et al. (2017), the miniaturization of electronics, along with reliability, increased performance, and cost reduction, has allowed the aerospace industry to develop and use small satellites. Pelton and Laufer (2019), highlighted the huge and rapid growth of the new commercial market related to microsats (10–100 kg) and minisats (100–500 kg), which are most frequently launched into low Earth orbits (LEO). Although 60% of the satellization missions of these small satellites employ medium-sized launch vehicles (LV), where they are carried out in a shared form such as "rideshare" or "piggyback", it has the disadvantage of waiting for launch opportunities, Wekerle et al. (2017). The use of small and Micro-LV to deploy small satellites offers some advantages. In this case, we can highlight greater flexibility in terms of the number of missions, specific orbits and, in some cases, shorter time to orbit, as well as technological development. Such characteristics guarantee the existence of a market opportunity for the employment of small and Micro-LV. In Kulu (2021), a market research of the launch industry in the employment of small launchers was presented.

The configuration of an LV will depend on the required performance, which in general is its ability to insert the mass of the satellite into orbit, Schlingloff (2005). To serve the Smallsat launch market in LEO we can mention the small LV, such as the Falcon1 (2008), Astra Rocket 4 (2020), Electron (2022) and Firefly Alpha (2016). All these LV are liquid propelled, Two-Stage to Orbit (TSTO), which present lower complexity, when compared to other multistage vehicles, with the minimum number of separation events, cost and the risk of failure, Motiwala et al. (2014). The use of liquid propulsion enables greater propulsive efficiency and control capacity in relation to solid propellant, Sutton and Blibarrz (2010).

In an LV with liquid propulsion, the dynamic behavior of the lateral sloshing of the propellants inside the tanks is a very important issue in their design, due to the stability and control conditions, Greensite (1970), Falangas (2016). Sloshing is defined as the periodic movement of the free surface of a liquid in a partially filled tank or container, Abramson (1966). The motion of the lateral sloshing waves has a natural frequency that depends on: (a) the shape of the tank and (b) the acceleration of gravity (in the laboratory) or the axial acceleration of the tank (for a launch vehicle under thrust), Dodge (2000). Propellant sloshing frequencies are usually lower than natural structural frequencies, but are sometimes close to the control system's bandwidth and can cause problems when it becomes unstable. Thus, the control system, flexible body and sloshing frequencies must be well separated. If the dominant frequencies of lateral sloshing are close to any of the control frequencies, it can result in an instability in the flight characteristics of the LV, whereas if the sloshing frequencies are close to the bending frequencies, a wide amplitude of oscillation can occur, Falangas (2016).

The study of the effects of lateral sloshing on the dynamic behavior of LV with respect to stability and control was well explored and documented in the 1960s in the development of NASA's Apollo project with Garner (1964), Bauer (1967) and Greensite (1967). The equations of motion of the LV are derived using the Lagrange´s method. To include sloshing effects in launcher dynamics, it is convenient to conceptually replace the liquid with an equivalent linear mechanical system, such as pendulum or mass-spring, as described in Abramson (1966), Dodge (2000) and Ibrahim (2005). For the dynamic analysis, the rigid and flexible body movement of the LV with the presence of the engine along with the effects of sloshing are considered. In this approach, we can cite the study by Nichawde et al. (2004) that evaluated the dynamic coupling between sloshing and rigid body of LV in atmospheric planar flight, using a sloshing model represented by a pendulum. The stability boundaries were analyzed with dimensionless parameters of the nonlinear model, as well as through root locus of the transfer functions of the linearized model. Following the same line, Shekhawat et al. (2006) applied bifurcation analysis techniques. The equations are linearized and root location graphs are obtained. The results show that the effect of sloshing can present static and dynamic instabilities in the vehicle. More recently, Pei (2021) analytically investigated the stability boundaries of sloshing in a space vehicle. He arrived at the same conclusion as Bauer (1967), that for a typical LV with thrust vector control and a single tank with sloshing, the danger zone of sloshing is located between the vehicle's center of mass (CG) and the center of percussion (CP), ignoring effects, such as aerodynamics and axial acceleration. If the sloshing mass is located between these two points mentioned, baffles may be required to provide additional damping for stability. Although this criterion is widely used, its application is limited to the analysis of sloshing stability for a single LV tank. Barrows and Orr (2021), stated that for two tanks, if the sloshing frequencies are well separated, Bauer's (1967) criterion can be applied. However, if they are too close, such an approach can lead to incorrect conclusions. The best approach in this case is to investigate stability through eigenvalues, obtaining the equations of motion arranged in a state space matrix form.

In the design and development of large and medium-sized LV with liquid propulsion, the study of sloshing should always be investigated, as the large amount of propellant mass can lead to stability and control problems. For the case of Micro-LV, this type of investigation can also gain importance, even involving a lower propellant mass. In this case, we can mention the LV Falcon 1, which during its second flight, an anomalous disturbance during the separation between the stages led to instabilities causing catastrophic loss, Bijelde et all (2007). It was later noted that the disturbance caused

instability due to sloshing in the second-stage tanks, which the control system was unable to handle. Changes in the tanks design, with the introduction of baffles rings, were adopted for the successive flights.

In the present work, a study of propellant sloshing effects in the stability of a Micro-LV TSTO during the ascending flight phase propelled by the first stage was performed. The sloshing was modelled by using mass-spring equivalent mechanical models. To overcome the lack of design data for this class of vehicles, the preliminary design of a concept vehicle was carried out. This design data can be useful as a benchmark for similar studies for other authors. The relationship between the instability caused by sloshing in the vehicle dynamics and the filling rate of the propellant tanks was investigated and the instability point identified. The use of ring baffles was proposed as a passive solution to mitigate unstable behavior.

2 MODEL

2.1 Sloshing

Sloshing is defined as the periodic motion of the free surface of a liquid in a partially filled tank or container. To analyze sloshing, it is conceptually convenient to replace the liquid with an equivalent linear mechanical system, such as a pendulum or mass-spring system, as described by Abramson (1966), Dodge (2000), and Ibrahim (2005).

2.1.1 Equivalent Mechanical Model

If the liquid is assumed as non-viscous and irrotational, its velocity distribution can be derived from the linear theory. The velocity potential of a mass of liquid undergoing sloshing and contained in a vertical cylindrical tank, according to Dodge (2000), for a typical self-solution and eigenvalues is given as:

$$\phi\left(r,z,\theta\right)=J_1\left(\lambda_{mn}\frac{2r}{d}\right)\cos\left(mn\theta\right)\frac{\cosh\left[\lambda_{mn}\frac{2\left(z+h\right)}{d}\right]}{\cosh\left(\lambda_{mn}\frac{2h}{d}\right)} \tag{1}$$

$$\Omega_{mn}^2=\lambda_{mn}\frac{2\overline{g}}{d}\tanh\left(\lambda_{mn}\frac{2h}{d}\right) \tag{2}$$

where r, θ, z are coordinates in a cylindrical coordinate system fixed to the tank, d is the tank diameter, h is the height of the liquid, λ_{mn}, are the zeros of the first kind Bessel function derivative and $\overline{g}$ is the axial acceleration of the tank (in the case of this work, it will be the axial acceleration of the Micro- LV). Sloshing modes can be symmetric or antisymmetric. When m=1 the antisymmetric modes of the surface waves are generated. Only antisymmetric modes generate forces and torques in the tanks. The values λ_{mn} for m=1 are denoted by ξ_n, whose values are: ξ_1=1.841, ξ_2=5.331, ξ_3=8.536, ξ_4=11.706, ξ_5=14.864, $\xi_{n1+1} \rightarrow \xi_{n1+1}= \xi_{n1}+\pi$.

To obtain the sloshing parameters of the mass-spring model, the static properties of the liquid must be preserved. Therefore, the sum of all the masses must be the same as the liquid mass m_{liq}, and the center of mass of the model must be at the same elevation as the liquid. These constraints are expressed analytically by:

$$\begin{aligned} m_0+\sum_{i=1}^{n}m_n &= m_{liq} \\ m_0h_0+\sum_{i=1}^{n}m_nh_n &= 0 \end{aligned} \tag{3}$$

where m_0 is the fixed mass and h_0 is distance of the fixed mass relative to the center of gravity of the tank (CG).

Additionally, the mechanical model must preserve the forces, torques, and natural frequencies. Figure 1 below illustrates the model parameters.

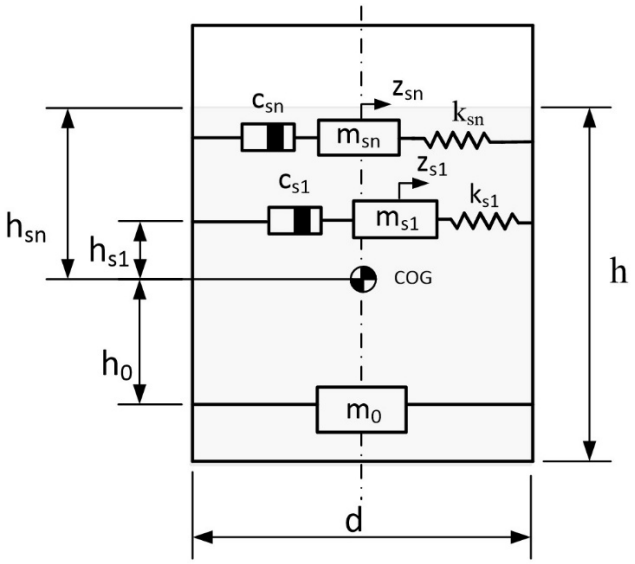


Figure 1 *Spring-mass model for the cylindrical tank.*

According to Abramson (1966), each of the spring constants k_{sn} is chosen in such a way that its ratio with the oscillating mass is equal to the square of the natural frequency, Ω_{sn}^2. Thus;

$$\Omega_{sn}^2 = \frac{k_{sn}}{m_{sn}} \tag{4}$$

where the parameters m_{sn} and k_{sn}, representing the slosh mass and its corresponding stiffness, respectively, and are calculated as follows:

$$m_{sn} = m_{liq}\left[\frac{d}{h\left(\xi_n^2 - 1\right)}\right]\tanh\left(2\frac{\xi_n h}{d}\right) \tag{5}$$

$$k_{sn} = m_{liq}\left[\frac{2\overline{g}}{h\left(\xi_n^2 - 1\right)}\right]\left[\tanh\left(2\frac{\xi_n h}{d}\right)\right]^2 \tag{6}$$

The constant c_{sn} refers to the sloshing damping, which may be attributed to the viscosity of the fluid, as well as an additional value provided by the baffles.

The distance between the sloshing mass and the CG of the tank is given as:

$$h_{sn} = \frac{h}{2} - \frac{d}{\xi_n}\tanh\left(\frac{\xi_n h}{d}\right) \tag{7}$$

and the expressions for determining the fixed mass and its position are, respectively,

$$m_0 = m_{liq} - \sum_{i=1}^{n} m_{s,i} h_{s,i} = 0 \tag{8}$$

$$h_0 = \frac{1}{m_0} - \sum_{i=1}^{n} m_{s,i} h_{s,i} = 0 \tag{9}$$

The total mass of the liquid is a function of the fill ratio (FR) of the tank and the density of the liquid, ρ_{liq},

$$m_{liq} = \frac{\pi}{4} d^2 h \, \rho_{liq} \tag{10}$$

Most propellant tanks on an LV have upper and lower elliptical domes, as shown in Figure 2. The parameters of an equivalent mechanical model for sloshing in a vertical cylindrical tank with a flat bottom cannot be directly applied to the dome area. One way to address this issue is to map a cylindrical tank with upper and lower domes to a cylindrical tank with flat top and bottom, while maintaining an equivalent liquid volume (Jang et al., 2013; Xin et al., 2018). Given a tank radius r_0, a dome depth h_d, height of the cylindrical part, h_b and total tank length od H, the expressions for the correction of the dome region according to Jang et al (2013) are given as:

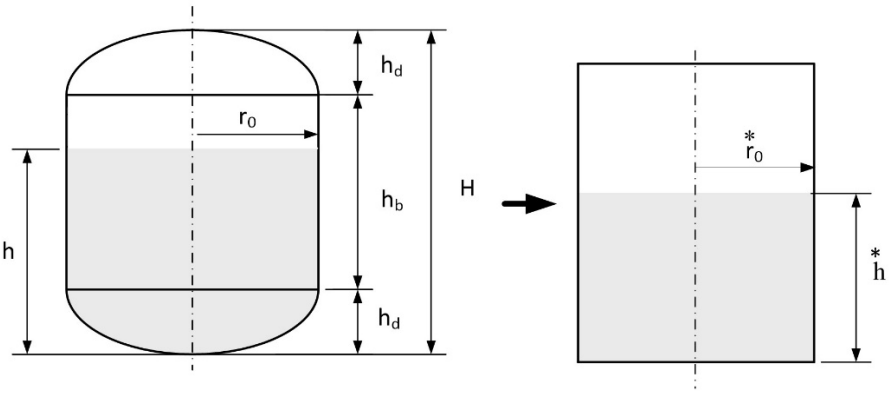


Figure 2 *Correction of the sloshing parameter for a cylindrical tank with elliptical domes, Jang et al (2013)*

For the case of liquid level in the upper dome area, the equivalent radius of the tank r_0^* and height of the liquid h^* for a cylindrical tank with a flat top and bottom can be derived as,

$$r_0^* = r_0 \sqrt{\frac{(H-h)(2h_d+h-H)}{h_d^2}}$$
$$h^* = \frac{2h_d^3 - 3Hh_d + (3h^2 - 6hH + 3H^2)h_d + h^3 - 3h^2H + 3hH^2 - H^3}{(6h_d - 6H)h_d + 3h^2 - 6hH + 3H^2} \tag{11}$$

When the liquid level is in the cylindrical section, as shown in Figure 2, the equivalent tank radius r_0^* and liquid height $h^*$for a cylindrical tank with a flat top and bottom can be derived as,

$$r_0^* = r_0$$
$$h^* = h - \frac{h_d}{3} \tag{12}$$

For the case of the liquid level in the lower dome area, the equivalent radius of the tank r_0^* and height of the liquid $h^*$for a cylindrical tank with a flat bottom can be derived as,

$$r_0^* = r_0\sqrt{\frac{h\left(2h_d - h\right)}{h_d^2}}$$
$$h^* = \frac{h\left(2h_d - h\right)}{6h_d - 3h} \tag{13}$$

2.1.2 Damping – ring baffles

It is known that damping caused solely by viscous effects is quite small; therefore, a method to add damping into the system may be necessary. It is also known that baffles provide a significant increase in damping when the liquid free surface is close to them.

In the work herein presentes, the damping provided by ring baffles is evaluated through the analogy of the drag exerted by a flat plate in an oscillatory flow, as analyzed by Miles (1958) and Dodge (2000). Figure 3 illustrates the schematic of the ring baffles, considering that the propellant oscillates in the fundamental sloshing mode, with the flow direction assumed to be normal to the ring. Damping calculations are given by Equation 14 below.

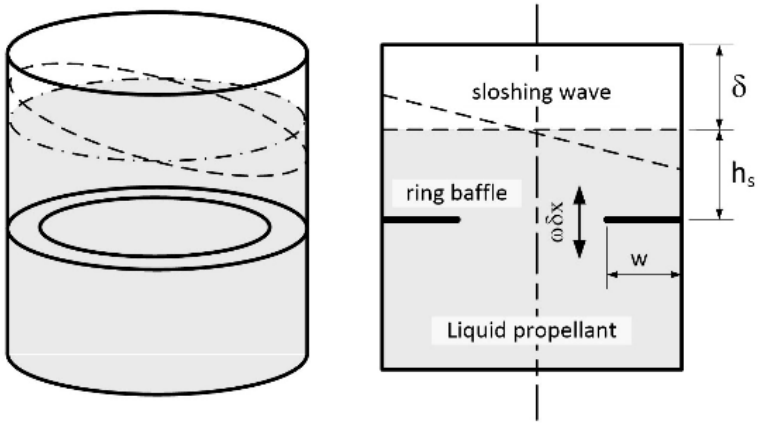


Figure 3 *Schematic of ring baffle with fundamental sloshing mode*

$$\gamma = 2.83\ e^{-4.6\left(h_s/r\right)} C_1^{3/2} \left(\delta\ /\ w\right)^{1/2} \tag{14}$$

where h_s is the depth of the damper relative to the free surface, r the radius of the tank, C_1 is the ratio of the damper area to the cross-sectional area of the tank, δ the amplitude of the wave of the first sloshing mode, and w is the width of the damper.

The damping γ decreases as the ring baffle is more submerged in relation to the free surface. For surface proximity effects, when the ring baffle is above the free surface for a distance equal to or greater than the amplitude of the sloshing, the sloshing wave does not intercept the damper and there is no damping. As the liquid level drops, the damping generated by the ring baffle approaches its maximum.

A ring baffle system must be designed to meet the design requirements. The damping provided by a ring baffle is non-linear, and the damping γ depends on the amplitude of sloshing δ as well as δ on γ. Therefore, efforts are made to establish the largest sloshing amplitude that can be reasonably assumed. A sloshing wave begins to exhibit noticeable nonlinearity when the amplitude exceeds approximately ten percent of the tank diameter. Consequently, the largest range of feasible sloshing that can be reasonably assumed is 0.2r (unless nonlinear effects can be analyzed), Dodge (2000). With a value of δ=0.2r, Equation (14) is reduced to:

$$\gamma = 1.27\ e^{-4.6\left(h_s/r\right)} C_1^{3/2} \tag{15}$$

were

$$C_1 \approx \frac{2w}{r} \tag{16}$$

The Equations (15) and (16) allow one to determine the spacing between the baffles to meet the specified minimum damping requirement for a given width of the dampers. Figure 4 displays the schematic design of the arrangement of the ring baffle within a tank. The graph on the left of this figure shows the predicted damping relative to the free surface. As can be seen, the minimum damping occurs when the free surface is slightly below (by 0.8δ) the nearest ring baffle

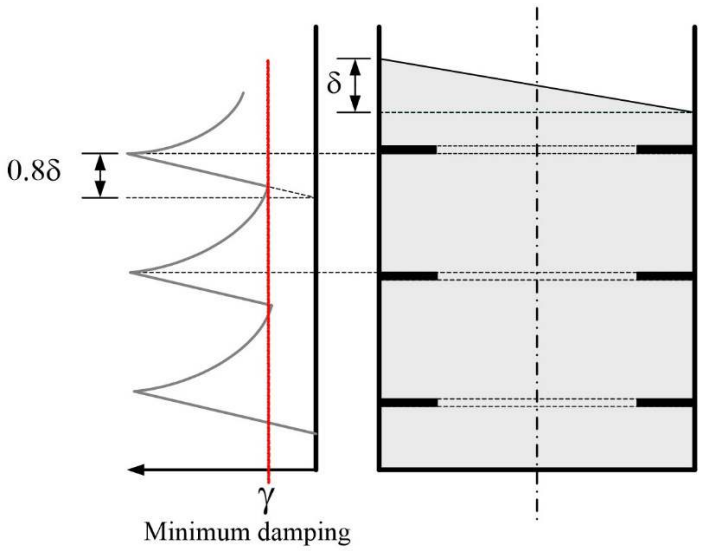


Figure 4 *Design of a ring baffle system, Dodge (2000)*

2.2 Dynamic structural model

The equation of motion of a discrete mechanical system with N degrees of freedom is given by, Craig and Kurdila (2006):

$$\mathbf{M}_B \ddot{\mathbf{z}}_B + \mathbf{C}_B \dot{\mathbf{z}}_B + \mathbf{K}_B \mathbf{z}_B = \mathbf{F} \tag{17}$$

We can then write the vector of displacements $\mathbf{z}_B$ as a function of the system modes that are stored in the columns of the matrix $\boldsymbol{\Psi}$ as:

$$\mathbf{z}_B = \boldsymbol{\Psi}\,\boldsymbol{\eta}(t) \tag{18}$$

Where $\boldsymbol{\eta}(t)$ are the generalized or modal coordinates. Substituting Equation (18) into Equation (17) yields:

$$\mathbf{M}_B \boldsymbol{\Psi} \ddot{\boldsymbol{\eta}} + \mathbf{C}_B \boldsymbol{\Psi} \dot{\boldsymbol{\eta}} + \mathbf{K}_B \boldsymbol{\Psi} \boldsymbol{\eta} = \mathbf{F} \tag{19}$$

Pre-multiplying all terms in the equation above by the transpose of matrix $\boldsymbol{\Psi}^T$ we obtain:

$$\boldsymbol{\Psi}^T \mathbf{M}_B \boldsymbol{\Psi}\, \ddot{\boldsymbol{\eta}} + \boldsymbol{\Psi}^T \mathbf{C}_B \boldsymbol{\Psi}\, \dot{\boldsymbol{\eta}} + \boldsymbol{\Psi}^T \mathbf{K}_B \boldsymbol{\Psi}\, \boldsymbol{\eta} = \boldsymbol{\Psi}^T \mathbf{F} \tag{20}$$

If the modes are normalized by the mass matrix, we have that:

$$\boldsymbol{\Psi}^{\mathrm{T}}\mathbf{M}_{\mathrm{B}}\boldsymbol{\Psi}=\mathbf{m}_{\mathrm{B}}=\mathbf{I} \tag{21}$$

$$\boldsymbol{\Psi}^{\mathrm{T}}\mathbf{K}_{\mathrm{B}}\boldsymbol{\Psi}=\boldsymbol{\Omega}_{\mathrm{B}}^{2} \tag{22}$$

If the damping is proportional, by substituting Equations (21) and (22) in (20) we obtain the equation of motion in generalized coordinates:

$$\ddot{\boldsymbol{\eta}}(\mathrm{t})+2\boldsymbol{\zeta}_{\mathrm{B}}\boldsymbol{\Omega}_{\mathrm{B}}\dot{\boldsymbol{\eta}}(\mathrm{t})+\boldsymbol{\Omega}_{\mathrm{B}}^{2}\boldsymbol{\eta}(\mathrm{t})=\mathbf{f}(\mathrm{t}) \tag{23}$$

where: $\mathbf{f}(t)=\boldsymbol{\Psi}^{T}\mathbf{F}(t)$ and the matrix $\boldsymbol{\zeta}_B$ contains on its principal diagonal the modal damping factors of the modes present in $\boldsymbol{\Psi}$.

2.3 Equations of motion of the launch vehicle

The equations of motion of an LV controlled by thrust vectoring at its rear, with liquid fuel tanks and an equivalent mass-spring-damper mechanical model to represent the sloshing motion in its tanks, are presented here. The equations of motion for an LV are derived by writing the equations for kinetic, potential, and dissipative energy and then applying Lagrange's equation (Garner, 1964; Greensite, 1970; Barrows and Orr, 2021). The Figure 5 shows the coordinate system used in the analysis. The coordinate axes $\mathbf{X}_I$, $\mathbf{Z}_I$ represent the stationary inertial system, while the axes $\mathbf{x}_b$,$\mathbf{z}_b$ represent the body system located at the CG of the LV. For simplicity, the motion of the LV is assumed to occur in the pitched plane given by $\mathbf{x}_b$,$\mathbf{z}_b$.

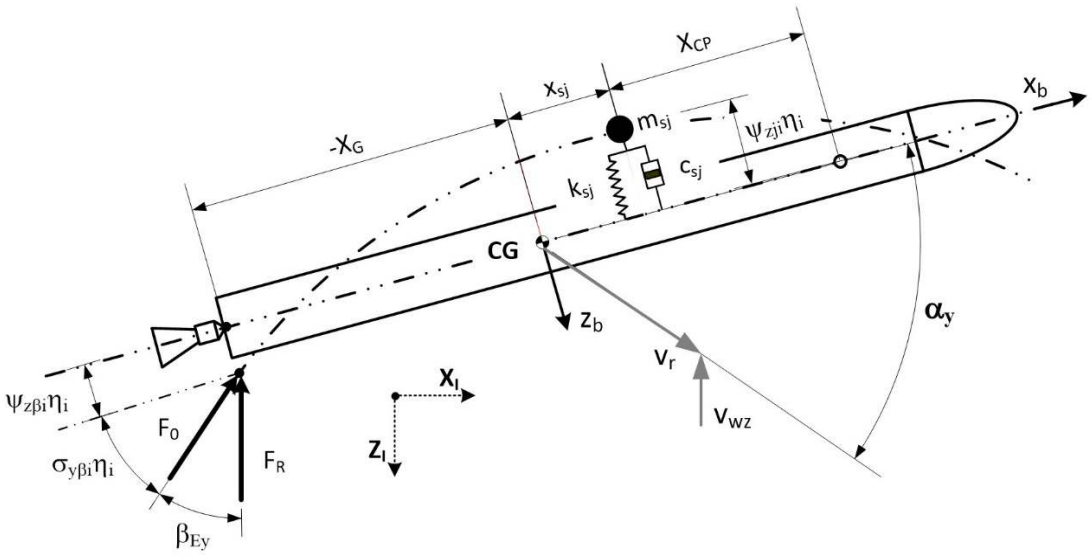


Figure 5 *Simplified Dynamic Model of the Flexible LV*

The linearized equations of motion produced by Barrows and Orr J. (2021) for translational, rotation, sloshing, and bending, are employed as presented below:

(a) Translation

$$\mathrm{M_T}\ddot{\mathrm{z}}_{\mathrm{I}}+\sum_{\mathrm{j}}\mathrm{m_{sj}}\ddot{\mathrm{z}}_{\mathrm{sj}}=-\mathrm{M_T}\,\bar{\mathrm{g}}\phi_{\mathrm{y}}-\mathrm{C_{N\alpha}}\,\bar{\mathrm{q}}\,\mathrm{S_{ref}}\left(\phi_{\mathrm{y}}+\frac{\dot{\mathrm{z}}_{\mathrm{I}}}{V}\right)-\mathrm{F}\sum_{\mathrm{i}}\sigma_{\mathrm{y\beta i}}\,\eta_{\mathrm{i}}-\mathrm{F_R}\,\beta_{\mathrm{Ey}}+\mathrm{S_E}\,\ddot{\beta}_{\mathrm{Ey}}\sum_{\mathrm{j}}\mathrm{m_{sj}}\ddot{\mathrm{z}}_{\mathrm{sj}}+\frac{\mathrm{C_{N\alpha}}\,\bar{\mathrm{q}}\,\mathrm{S_{ref}}}{\mathrm{V}}\mathrm{V_{wz}} \tag{24}$$

where M_T is the total mass of the vehicle (including engines and the sloshing mass), $\ddot{z}_I$ is the inertial acceleration in the z-direction, m_{sj} is sloshing mass of the j^{th} tank, $\ddot{z}_{sj}$ the sloshing acceleration of the j^{th} tank, $\bar{g}$ is the longitudinal sensed

acceleration, ϕ_y, is the pitch angle of the undeformed centerline relative to the trajectory frame, $C_{N\alpha}$, is the aerodynamic normal force coefficient slope , $\bar{q}$ is the dynamic pressure, S_{ref} is the reference aerodynamic area,), $\dot{z}_I$ is the inertial velocity in the z-direction, V is the absolute relative velocity, F is the thrust of all engines,$\sigma_{y\beta i}$ is the rotation mode about pitch axis at the gimbal position,η_i is the displacement amplitude of i^{th} flexible mode, F_R is the thrust of gimbaled engines,β_{Ey} is the engine angle about the pitch axis, S_E is the first moment of inertia of engine about its gimbal(expressed in engine frame), $\ddot{\beta}_{Ey}$ is the engine angular acceleration about pitch axis and V_{wz} is the velocities of the wind in the z-direction .

The acceleration $\bar{g}$ is expressed as:

$$\overline{\mathrm{g}}=\frac{(\mathrm{F}-\mathrm{D})}{\mathrm{M_T}} \tag{25}$$

Where D is the drag force expressed as:

$$\mathrm{D}=\mathrm{C_d}\,\overline{\mathrm{q}}\,\mathrm{S_{ref}} \tag{26}$$

where C_d is the drag coefficient.

(b) Rotation

$$\begin{aligned}\dot{\omega}_{\mathrm{y}}\,\mathrm{I_{yy}}-\sum_{\mathrm{j}}\mathrm{m_{sj}}\,\mathrm{x_{sj}}\,\ddot{\mathrm{z}}_{\mathrm{sj}}=&-\sum_{j}\mathrm{m_{sj}}\,\overline{\mathrm{g}}\,\mathrm{z_{sj}}+\mathrm{C_{N\alpha}}\,\overline{\mathrm{q}}\,\mathrm{S_{ref}}\,\mathrm{X_{cp}}\left(\phi_{\mathrm{y}}+\frac{\dot{\mathrm{z}}_{\mathrm{I}}}{\mathrm{V}}\right)+\mathrm{X}_{G}\left(\mathrm{F_R}\,\beta_{\mathrm{Ey}}+\mathrm{F}\sum_{i}\sigma_{\mathrm{y\beta i}}\,\eta_{\mathrm{i}}\right)\\&+\mathrm{F}\sum_{i}\psi_{\mathrm{z\beta i}}\,\eta_{\mathrm{i}}+\left(\mathrm{X_G\,S_E}-\mathrm{I_{EG}}\right)\ddot{\beta}_{\mathrm{Ey}}-\mathrm{X_{cp}}\,\frac{\mathrm{C_{N\alpha}}\,\overline{\mathrm{q}}\,\mathrm{S_{ref}}}{\mathrm{V}}\,\mathrm{V_{wz}}\end{aligned} \tag{27}$$

where $\dot{\omega}_y$ is the angular acceleration of the body, I_{yy}, is the moment of inertia of the LV (including motors and sloshing mass) with respect to the origin, x_{sj} is the equilibrium position of the sloshing mass in x-direction, z_{sj}, the sloshing displacement of the j^{th} tank, X_{CP} is the center of pressure measured from the origin, X_G is the gimbal coordinate, $\psi_{z\beta i}$, is the z-bending mode shape of i^{th} mode at gimbal, I_{EG} is the moment of inertia of engine about the gimbal center.

(c) Sloshing

$$\ddot{\mathrm{z}}_{\mathrm{sj}}+2\zeta_{\mathrm{sj}}\Omega_{\mathrm{sj}}\dot{\mathrm{z}}_{\mathrm{sj}}+\Omega_{\mathrm{sj}}^{2}\mathrm{z_{sj}}=-\ddot{\mathrm{z}}_{\mathrm{I}}-\overline{\mathrm{g}}\phi_{\mathrm{y}}+\mathrm{x_{sj}}\ddot{\phi}_{\mathrm{y}}-\sum_{\mathrm{j}}\psi_{\mathrm{zji}}\,\ddot{\eta}_{\mathrm{i}} \tag{28}$$

Where ζ_{sj} is the sloshing damping factor of the j^{th} tank, Ω_{sj} is the sloshing natural frequency of the j^{th} tank, $\dot{z}_{sj}$ the velocity sloshing of the j^{th} tank, $\ddot{\phi}_y$ is the angular acceleration of the body, $\ddot{\eta}_i$ is the acceleration amplitude of i^{th} flexible mode.

(d) Bending

$$\left(\ddot{\eta}_{\mathrm{i}}+2\zeta_{\mathrm{Bi}}\Omega_{\mathrm{Bi}}\dot{\eta}_{\mathrm{i}}+\Omega_{\mathrm{Bi}}^{2}\eta_{\mathrm{i}}\right)\mathrm{m_{Bi}}=-\overline{\mathrm{q}}\,\mathrm{S_{ref}}\;\mathrm{C_{N\eta i}}\,\alpha_{\mathrm{y}}-\sum_{\mathrm{j}}\mathrm{m_{sj}}\,\psi_{\mathrm{zji}}\,\ddot{\mathrm{z}}_{\mathrm{sj}}+\psi_{\mathrm{zBi}}\ddot{\beta}_{\mathrm{Ey}}\,\mathrm{S_{EX}}-\sigma_{\mathrm{zBi}}\,\ddot{\beta}_{\mathrm{Ez}}\,\mathrm{I_{EG}}-\mathrm{F_R}\,\psi_{\mathrm{zBi}}\,\beta_{\mathrm{Ey}}\,\mathrm{S_{EX}} \tag{29}$$

Where ζ_{Bi} the damping factor of i^{th} bending mode, Ω_{Bi} natural frequency of the i^{th} bending mode, $\dot{\eta}_i$ is the velocity amplitude of i^{th} flexible mode,ψ_{zji} is the z-bending mode shape of the i^{th} mode at the slosh location and $C_{N\eta i}$ is the aerodynamic coefficient of bending, expressed as:

$$C_{N\eta i} = \int \frac{\partial C_{N\alpha}}{\partial x} \psi_{zi} \, dx \tag{30}$$

where ($cC_{N\alpha}/cx$) represents the derivative of the normal force coefficient along the length of the LV.

2.4 Equation of motion in a state space form

The equation of motion for a linear system in state space form is given by:

$$\mathbf{E}\dot{\mathbf{x}} = \mathbf{A}\mathbf{x} + \mathbf{B}\mathbf{u} \tag{31}$$

$$\mathbf{y} = \mathbf{C}\mathbf{x} + \mathbf{D}\mathbf{u} \tag{32}$$

and the first equation can be solved to an explicit system of linear equations,

$$\dot{\mathbf{x}} = \underbrace{\mathbf{E}^{-1}\mathbf{A}}_{\tilde{\mathbf{A}}} \mathbf{x} + \underbrace{\mathbf{E}^{-1}\mathbf{B}}_{\tilde{\mathbf{B}}} \mathbf{u} \tag{33}$$

where the matrix $\mathbf{E}$ contains the mass and inertia parameters of the system. The matrix $\tilde{\mathbf{A}}$, $\tilde{\mathbf{B}}$, $\mathbf{C}$ and $\mathbf{D}$ can be used in the design of control systems and stability analysis.

The state vector of the system comprises the rigid body states of the LV, the sloshing states of the propellant, and the generalized elastic coordinates, such that,

$$\mathbf{x} = \begin{bmatrix} \mathbf{x}_r \\ \mathbf{x}_s \\ \mathbf{x}_f \end{bmatrix} \tag{34}$$

where $\mathbf{x}_r$ is the rigid body state vector, $\mathbf{x}_s$ is the sloshing state vector, and $\mathbf{x}_f$ is the bending state vector. These state vectors are given by,

$$\mathbf{x}_r = \begin{bmatrix} \phi_y & \omega_y & \dot{z}_I \end{bmatrix} \tag{35}$$

$$\mathbf{x}_s = \begin{bmatrix} z_{s1} & \cdots & z_{sN} & \dot{z}_{s1} & \cdots & \dot{z}_{sN} \end{bmatrix}^T \tag{36}$$

$$\mathbf{x}_f = \begin{bmatrix} \eta_1 & \cdots & \eta_{1M} & \dot{\eta}_1 & \cdots & \dot{\eta}_{1M} \end{bmatrix}^T \tag{37}$$

The inputs consist of β_{Ey} , $\ddot{\beta}_{Ey}$ and V_{wz} , described previously. Therefore, we have:

$$\mathbf{u} = \begin{bmatrix} \beta_{Ey} & \ddot{\beta}_{Ey} & V_{wz} \end{bmatrix} \tag{38}$$

The integral form of the model given by Equation (31) with its submatrices is expressed as:

$$\begin{bmatrix}\mathbf{E}_{\mathrm{r}}\\ \mathbf{E}_{\mathrm{s}}\\ \mathbf{E}_{\mathrm{f}}\end{bmatrix}\begin{bmatrix}\dot{\mathbf{x}}_{\mathrm{r}}\\ \dot{\mathbf{x}}_{\mathrm{s}}\\ \dot{\mathbf{x}}_{\mathrm{f}}\end{bmatrix}=\begin{bmatrix}\mathbf{A}_{\mathrm{r}} & \mathbf{A}_{\mathrm{rs}} & \mathbf{A}_{\mathrm{rf}}\\ \mathbf{A}_{\mathrm{sr}} & \mathbf{A}_{\mathrm{s}} & \mathbf{A}_{\mathrm{sf}}\\ \mathbf{A}_{\mathrm{fr}} & \mathbf{A}_{\mathrm{fs}} & \mathbf{A}_{\mathrm{f}}\end{bmatrix}\begin{bmatrix}\mathbf{x}_{\mathrm{r}}\\ \mathbf{x}_{\mathrm{s}}\\ \mathbf{x}_{\mathrm{f}}\end{bmatrix}+\begin{bmatrix}\mathbf{B}_{\mathrm{r}}\\ \mathbf{B}_{\mathrm{s}}\\ \mathbf{B}_{\mathrm{f}}\end{bmatrix}\mathbf{u} \tag{39}$$

According to Barrows and Orr (2021), in order to facilitate the conversion of equations into matrix for, the equations of motion were grouped first by the dynamic terms followed by the inputs. The accelerations are placed on the left side of the equations, followed by the velocities and displacements on the right side of the equations, followed finally by the inputs. It is assumed that $\mathbf{m}_{\mathrm{B}}=\mathbf{I}$. It is important to note that for small disturbances $\dot{\phi}_y=\omega_{\mathrm{y}}$.

Next, the submatrices of Equation (39) are presented for an LV with two fundamental sloshing modes, one for each tank, and three bending modes, which is considered sufficient according to Greensite (1970).

Submatrices of **E** :

$$\mathbf{E}_{\mathrm{r}}=\begin{bmatrix}1 & 0 & 0 & 0 & 0 & 0 & 0 & 0 & 0 & 0 & 0 & 0\\ 0 & \mathrm{I}_{\mathrm{yy}} & 0 & 0 & 0 & -\mathrm{x}_{\mathrm{s1}}\mathrm{m}_{\mathrm{s1}} & -\mathrm{x}_{\mathrm{s2}}\mathrm{m}_{\mathrm{s2}} & 0 & 0 & 0 & 0 & 0 & 0\\ 0 & 0 & \mathrm{M}_{\mathrm{T}} & 0 & 0 & \mathrm{m}_{\mathrm{s1}} & \mathrm{m}_{\mathrm{s2}} & 0 & 0 & 0 & 0 & 0 & 0\end{bmatrix} \tag{40}$$

$$\mathbf{E}_{\mathrm{s}}=\begin{bmatrix}0 & 0 & 0 & 1 & 0 & 0 & 0 & 0 & 0 & 0 & 0 & 0 & 0\\ 0 & 0 & 0 & 0 & 1 & 0 & 0 & 0 & 0 & 0 & 0 & 0 & 0\\ 0 & -\mathrm{x}_{\mathrm{s1}} & 1 & 0 & 0 & 1 & 0 & 0 & 0 & 0 & \psi_{\mathrm{z11}} & \psi_{\mathrm{z12}} & \psi_{\mathrm{z13}}\\ 0 & -\mathrm{x}_{\mathrm{s2}} & 1 & 0 & 0 & 0 & 1 & 0 & 0 & 0 & \psi_{\mathrm{z21}} & \psi_{\mathrm{z22}} & \psi_{\mathrm{z23}}\end{bmatrix} \tag{41}$$

$$\mathbf{E}_{\mathrm{f}}=\begin{bmatrix}0 & 0 & 0 & 0 & 0 & 0 & 0 & 1 & 0 & 0 & 0 & 0\\ 0 & 0 & 0 & 0 & 0 & 0 & 0 & 0 & 1 & 0 & 0 & 0\\ 0 & 0 & 0 & 0 & 0 & 0 & 0 & 0 & 0 & 1 & 0 & 0\\ 0 & 0 & 0 & \mathrm{m}_{\mathrm{s1}}\psi_{\mathrm{z11}} & \mathrm{m}_{\mathrm{s2}}\psi_{\mathrm{z21}} & 0 & 0 & 0 & 0 & 0 & 1 & 0\\ 0 & 0 & 0 & \mathrm{m}_{\mathrm{s1}}\psi_{\mathrm{z12}} & \mathrm{m}_{\mathrm{s2}}\psi_{\mathrm{z22}} & 0 & 0 & 0 & 0 & 0 & 0 & 1\\ 0 & 0 & 0 & \mathrm{m}_{\mathrm{s1}}\psi_{\mathrm{z13}} & \mathrm{m}_{\mathrm{s2}}\psi_{\mathrm{z23}} & 0 & 0 & 0 & 0 & 0 & 0 & 0\end{bmatrix} \tag{42}$$

Submatrices of **A** :

$$\mathbf{A}_{\mathrm{r}}=\begin{bmatrix}0 & 1 & 0\\ \mathrm{C}_{\mathrm{N}\alpha}\overline{\mathrm{q}}\,\mathrm{S}_{\mathrm{ref}}\mathrm{X}_{\mathrm{CP}} & 0 & \left(\mathrm{C}_{\mathrm{N}\alpha}\overline{\mathrm{q}}\,\mathrm{S}_{\mathrm{ref}}/\mathrm{V}\right)\mathrm{X}_{\mathrm{CP}}\\ -\mathrm{M}_{\mathrm{T}}\overline{\mathrm{g}}-\mathrm{C}_{\mathrm{N}\alpha}\overline{\mathrm{q}}\,\mathrm{S}_{\mathrm{ref}} & 0 & -\left(\mathrm{C}_{\mathrm{N}\alpha}\overline{\mathrm{q}}\mathrm{S}_{\mathrm{ref}}/\mathrm{V}\right)\end{bmatrix} \tag{43}$$

$$\mathbf{A}_{\mathrm{rs}}=\begin{bmatrix}0 & 0 & 0 & 0\\ -\overline{\mathrm{g}}\,\mathrm{m}_{\mathrm{s1}} & -\overline{\mathrm{g}}\,\mathrm{m}_{\mathrm{s2}} & 0 & 0\\ 0 & 0 & 0 & 0\end{bmatrix} \tag{44}$$

$$\mathbf{A}_{\mathrm{rf}}=\begin{bmatrix}0 & 0 & 0 & 0 & 0 & 0\\ \mathrm{F}\left(\mathrm{X}_{\mathrm{G}}\sigma_{\mathrm{y\beta1}}+\psi_{\mathrm{z\beta1}}\right) & \mathrm{F}\left(\mathrm{X}_{\mathrm{G}}\sigma_{\mathrm{y\beta2}}+\psi_{\mathrm{z\beta2}}\right) & \mathrm{F}\left(\mathrm{X}_{\mathrm{G}}\sigma_{\mathrm{y\beta3}}+\psi_{\mathrm{z\beta3}}\right) & 0 & 0 & 0\\ -\mathrm{F}\sigma_{\mathrm{y\beta1}} & -\mathrm{F}\sigma_{\mathrm{y\beta2}} & -\mathrm{F}\sigma_{\mathrm{y\beta3}} & 0 & 0 & 0\end{bmatrix} \tag{45}$$

$$\mathbf{A}_{s} = \begin{bmatrix} 0 & 0 & 1 & 0 \\ 0 & 0 & 0 & 1 \\ -\Omega_{s1}{}^{2} & 0 & -2\zeta_{s1}\Omega_{s1} & 0 \\ 0 & -\Omega_{s2}{}^{2} & 0 & -2\zeta_{s2}\Omega_{s2} \end{bmatrix} \tag{46}$$

$$\mathbf{A}_{sr} = \begin{bmatrix} 0 & 0 & 0 \\ 0 & 0 & 0 \\ -\overline{g} & 0 & 0 \\ -\overline{g} & 0 & 0 \end{bmatrix} \tag{47}$$

$$\mathbf{A}_{f} = \begin{bmatrix} 0 & 0 & 0 & 1 & 0 & 0 \\ 0 & 0 & 0 & 0 & 1 & 0 \\ 0 & 0 & 0 & 0 & 0 & 1 \\ -\Omega_{B1}{}^{2} & 0 & 0 & -2\zeta_{B1}\Omega_{B1} & 0 & 0 \\ 0 & -\Omega_{B2}{}^{2} & 0 & 0 & -2\zeta_{B2}\Omega_{B2} & 0 \\ 0 & 0 & -\Omega_{B3}{}^{2} & 0 & 0 & -2\zeta_{B3}\Omega_{B3} \end{bmatrix} \tag{48}$$

$$\mathbf{A}_{sf} = \begin{bmatrix} 0 & 0 & 0 & 0 & 0 & 0 \\ 0 & 0 & 0 & 0 & 0 & 0 \\ 0 & 0 & 0 & 0 & 0 & 0 \\ 0 & 0 & 0 & 0 & 0 & 0 \end{bmatrix} \tag{49}$$

$$\mathbf{A}_{fr} = \begin{bmatrix} 0 & 0 & 0 \\ 0 & 0 & 0 \\ 0 & 0 & 0 \\ -\left(\overline{q}\,S_{ref}C_{N\eta 1}\right) & 0 & -\left(\overline{q}\,S_{ref}C_{N\eta 1}\right)/V \\ -\left(\overline{q}\,S_{ref}C_{N\eta 2}\right) & 0 & -\left(\overline{q}\,S_{ref}C_{N\eta 2}\right)/V \\ -\left(\overline{q}\,S_{ref}C_{N\eta 3}\right) & 0 & -\left(\overline{q}\,S_{ref}C_{N\eta 3}\right)/V \end{bmatrix} \tag{50}$$

$$\mathbf{A}_{fr} = \mathbf{A}_{fr}{}^{T} \tag{51}$$

Submatrices of **B** :

$$\mathbf{B}_{r} = \begin{bmatrix} 0 & 0 & 0 \\ F_{R}X_{G} & \left(S_{E}X_{G} - I_{EG}\right) & -\left(C_{N\alpha}\overline{q}\,S_{ref}X_{CP}\right)/V \\ -F_{R} & S_{E} & \left(C_{N\alpha}\overline{q}\,S_{ref}\right)/V \end{bmatrix} \tag{52}$$

$$\mathbf{B}_s = \begin{bmatrix} 0 & 0 & 0 \\ 0 & 0 & 0 \\ 0 & 0 & 0 \\ 0 & 0 & 0 \end{bmatrix} \tag{53}$$

$$\mathbf{B}_f = \begin{bmatrix} 0 & 0 & 0 \\ 0 & 0 & 0 \\ 0 & 0 & 0 \\ -\left(F_R\,\psi_{z\beta 1}\right) & \left(\psi_{z\beta 1} S_E - \sigma_{y\beta 1} I_{EG}\right) & \left(\overline{q}\,S_{ref} C_{N\eta 1}\right)/V \\ -\left(F_R\,\psi_{z\beta 2}\right) & \left(\psi_{z\beta 2} S_E - \sigma_{y\beta 2} I_{EG}\right) & \left(\overline{q}\,S_{ref} C_{N\eta 2}\right)/V \\ -\left(F_R\,\psi_{z\beta 3}\right) & \left(\psi_{z\beta 3} S_E - \sigma_{y\beta 3} I_{EG}\right) & \left(\overline{q}\,S_{ref} C_{N\eta 3}\right)/V \end{bmatrix} \tag{54}$$

The matrices **C** and **D** below are arranged to determine the transfer function between the pitch angle ϕ_y and the gimbal angle of the engine β_{Ey}, in order to analyze the stability of the LV with sloshing effects

$$\mathbf{C} = \begin{bmatrix} 1 & 0 & 0 & 0 & 0 & 0 & 0 & 0 & 0 & 0 & 0 & 0 & 0 \end{bmatrix} \tag{55}$$

$$\mathbf{D} = \begin{bmatrix} 0 & 0 & 0 \end{bmatrix} \tag{56}$$

2.5 Stability

The simplest control law required to stabilize the attitude of an LV, without damping in pitch, is known as proportional-derivative (PD) control. Its control law can be expressed in the following form, as described by Barrows and Orr (2021):

$$\beta_e = -k_p \phi_y - k_D \dot{\phi}_y \tag{57}$$

where β_e is the gimbal angle of the engine, for open-loop stability analysis, ϕ_y the pitch angle, $\dot{\phi}_y$ its rate of change. The gain k_p (proportional gain) and k_D (the gain derivative), determined according to Barrows and Orr (2021), such as:

$$k_p = \frac{I_{yy}\,\omega_c^2 + C_{N\alpha}\,\overline{q}\,S_{ref}\,X_{CP}}{-X_G\,F_R} \tag{58}$$

$$k_D = \frac{I_{yy}\,\zeta_c\,\omega_c}{-X_G\,F_R} \tag{59}$$

Where ω_c and ζ_c are the frequency and control damping ratios, respectively, that meet the design criteria. These parameters can be optimized according to the performance index.

One of the results obtained by Bauer (1967) and Greensite (1970) is the determination of a region defined as a danger zone, for a LV without aerodynamic effects, with PD attitude control with a single dominant slosh mass. Therefore, if the slosh mass is located between the center of gravity (CG) and the center of percussion (CP) of the LV, instability will occur. For systems with two or more tanks, with frequencies close enough to dynamically couple, this result does not necessarily hold. However, it is still a good guideline to check which tanks have the sloshing mass located in that region

in order to predict the need for dampers for greater liquid propellant damping, Ottander et al. (2018). According to Greensite (1970), the center of percussion of an LV, Figure 6, is determined as:

$$C_P = \frac{I_{YY}}{X_G M_T} \tag{60}$$

where I_{yy}, X_G and M_T are described in Section 2.3.

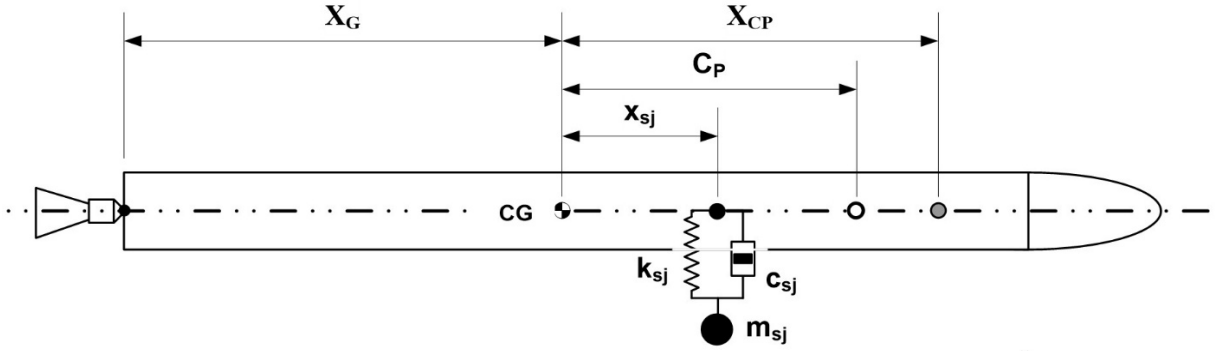


Figure 6 *Danger zone*

According to Pei (2021), if the sloshing mass is within the danger zone, the rigid body control condition becomes unfavorable. In this case, the control actuator indirectly adds energy to the sloshing mode while attempting to control the attitude of the rigid body.

Figure 7 highlights the difference between a stable and unstable sloshing mode in a *root locus* plot. In a stable scenario, the natural frequency Ω_p of sloshing pole is greater than zero, and the angle of departure is directed toward the left half-plane (LHP), Figure 7(a). Thus, the closed-loop sloshing pole is stable for all values of the feedback gains. In an unstable scenario, the sloshing pole is below zero and the angle of departure is directed toward the right half-plane (RHP), Figure 7(b). Additional damping is required to shift the root locus to the LHP, ensuring that the closed-loop sloshing pole remains stable, as depicted in Figure 7(c). In a design case, damping can be introduced through the use of baffles.

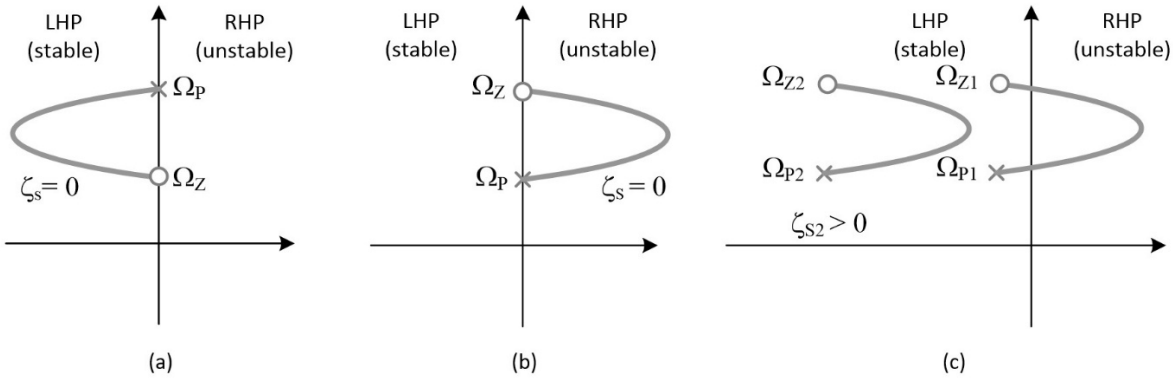


Figure 7 *Root locus illustration: (a) stable sloshing mode (b) unstable sloshing mode (c) stabilization with increased damping*

3 CONCEPTUAL LAUNCHER VEHICLE

3.1 Definition

In order to carry out the analyses on the effect of sloshing on the stability of a Micro-LV proposed for this work, it was decided to develop a conceptual LV of this category, since most of the data related to launch vehicles is confidential.

Sizing a launch vehicle can involve many different approaches and employ a variety of mass estimation techniques Edberg and Costa (2022). The strategy employed in this work uses a top-down approach involving the ideal propellant and structural masses for each stage of the LV (based on initial assumptions), designing the inert mass components of

each stage (tanks, engines, etc.) and then comparing their masses with those initially estimated, analyzing the performance through the approximate calculation of the trajectory, in order to determine feasibility. Some iterations are then carried out until a satisfactory design solution is reached, Motiwala et.al (2014)

3.2 Speed Requirements

The velocity requirement for space launch systems, termed Δv, is the result of the difference between the initial velocity and the terminal velocity. To determine the speed acquired by a rocket in an environment free of aerodynamics and gravitational forces, Tsiolkovsky's equation can be used, Edberg and Costa (2022),

$$\Delta v = v_e \ln\left(\frac{m_0}{m_f}\right) = g_0 \, Isp \ln\left(\frac{m_0}{m_f}\right) \tag{61}$$

where Δv is the acquired velocity, v_e is the effective exhaust velocity of the gases from the nozzle, m_0 is the initial mass and m_f is the final mass, g_0=9.80665 (m/s^2) and I_{SP} is the specific impulse. In this way, the LV will acquire the highest velocity when all the propellant is consumed.

However, during the ascent flight phase, the LV is subjected to opposing forces. The most significant are the gravitational and aerodynamic force, so we have:

$$\Delta v_{losses} = \Delta v_{grav} + \Delta v_{drag} \tag{62}$$

Considering a circular orbit, the terminal velocity for the payload to remain in orbit, it is given by Edberg and Costa (2022), as:

$$v_{orbit} = \sqrt{\frac{g_0 R^2}{R+h}} \tag{63}$$

where R=6378 km is the Earth ‘s average radios, and h is the elevation of the orbit.

Thus, this leads to an ideal or design velocity given by:

$$\Delta v_{idelal} = g_0 \, Isp \ln\left(\frac{m_0}{m_f}\right) = \Delta v_{orbit} + \Delta v_{losses} \tag{64}$$

3.3 Launch Vehicle Parameters

The process for calculating the mass of an LV begins with determining the basic parameters of the vehicle. We will assume that the following quantities have been provided or selected for each stage.

From Equation 61, we can define the parameter μ as a mass ratio in the form:

$$\mu = \left(\frac{m_0}{m_f} = \frac{m_0}{m_0 - m_p}\right) = \frac{m_s + m_p + m_0 - m_{PL}}{m_s - m_{PL}} \tag{65}$$

Where m_s is the structural mass or inert mass, m_p the propellant mass and m_{PL} the payload mass.

Another necessary parameter consists of the structural mass factor defined as:

$$\sigma = \frac{m_s}{m_s + m_p} = \frac{m_s}{m_0 - m_p} \tag{66}$$

For a multistage LV, it is assumed that for each stage values of Δv, I_{SP} and σ , are necessary for independent calculations. It should be considered that the payload for the k^{th} stage of N stages is the sum of the masses of the fully loaded stages above the k^{th} stage and the payload. In such a way:

$$m_{PL1} = \left(m_{s2} + m_{p2}\right) + \left(m_{s3} + m_{p3}\right) + \ldots + \left(m_{sN} + m_{pN}\right) + m_{PL} \tag{67}$$

By substituting Equation (65) into Equation (64), to find the mass ratio of the μ uppermost stage such that:

$$\mu = e^{\left(\frac{\Delta v_{ideal}}{g_0 Isp}\right)} \tag{68}$$

One can calculate the mass of the propellant m_p as:

$$m_p = m_{PL} \frac{(\mu - 1)(1 - \sigma)}{1 - \sigma\,\mu} \tag{69}$$

In this way, the structural or inert mass m_s is then calculated:

$$m_s = m_p \frac{\sigma}{(1 - \sigma)} \tag{70}$$

This process is repeated for each of the vehicle's stages, until the first stage is reached.

Another parameter required for LV sizing consists of the rocket thrust-to-weight ratio which is equal to the total thrust produced divided by the total mass of the rocket:

$$\frac{T}{W} = \frac{T}{g_0 m} \tag{71}$$

To make the rocket take off possible the ratio, (T/W) must be larger than 1.

3.4 Design considerations

A conceptual Two-Stage to Orbit (TSTO) Micro-LV was implemented. This configuration has lower complexity when compared to other multi-stage LV due to the minimum number of separation events, cost, and risk of failure. Design characteristics were derived from similar Micro-LV, such as Falcon 1 (2008), Astra (2022), Electron (2020), and Firefly Alpha (2016), as well as the launch vehicle presented in Zuhang and Yuli (2021). It was assumed that the vehicle will be launched from the Alcântara Space Center (CEA) with latitude of 2.3°S and longitude of 44.4° W in a circular Low Earth Orbit (LEO) of 300 (km) altitude and inclination of 51.6° with a payload mass of 100 (kg). Other assumptions include, I_{SP}, σ,μ,T/W and number of engines for each stage. Table 1 presents the initial parameters of the Micro-LV, where Ø is assumed diameter.

Table 1 Micro-LV initial design parameter

Stage	Propellant	Isp (s)	T (kN)	T/W	σ	μ	Engines	Ø (m)
1	*LOX / RP-1	291.0	165	1.3	0.09	3.28	1	1.0
2	**LOX / RP-1**	**321.8**	**17.7**	**0.6**	**0.11**	**7.35**	**1**	**1.0**
* LOX (oxidizer) and RP-1 (fuel:)								

4 RESULTS

4.1 Conceptual vehicle

The defined parameters are used to complete the design. Mission requirements are met with an optimized trajectory calculation. Table 2 presents the final data for the respective Micro-LV stages and Figure 8 shows the defined dimensions.

Table 2 Launch Vehicle Parameters

Stage	Propellant	I_{SP} (s)	T (kN)	T/W	*MR	m_p (kg)	m_s (kg)	Δv (km/s)	Engines
1	LOX / RP-1	291.0	165	1.3	2.4	8727.68	846.28	2.04	1
2	LOX / RP-1	321.8	17.7	0.6	2.4	2573.54	305.35	5.20	1

*MR: mixture ratio (O/F).

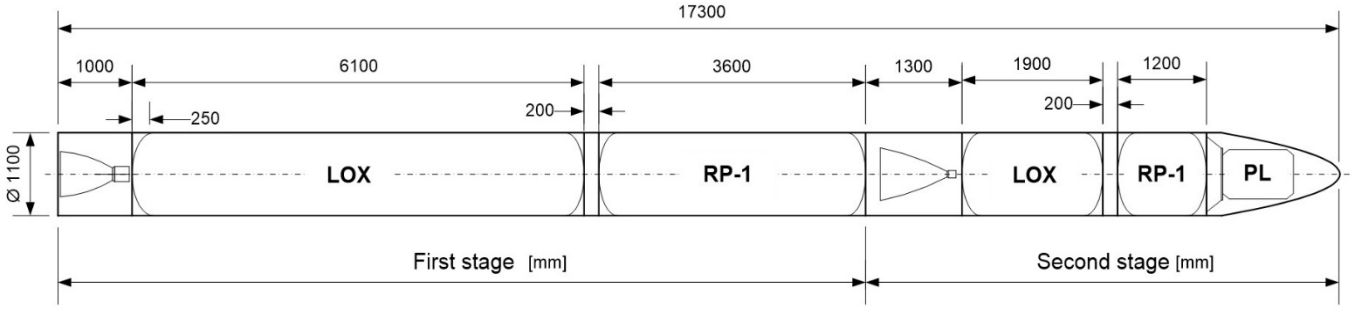


Figure 8 *Layout of Micro-LV*

The aerodynamic coefficients, Figure 9, were calculated for the flight of the first stage by using the Missile Datcom software, Blake (1998). The cross-section area of the Micro-LV was considered as the reference S_{ref}. The ogive nose was selected due to its lower drag cofficiets in flight regimes

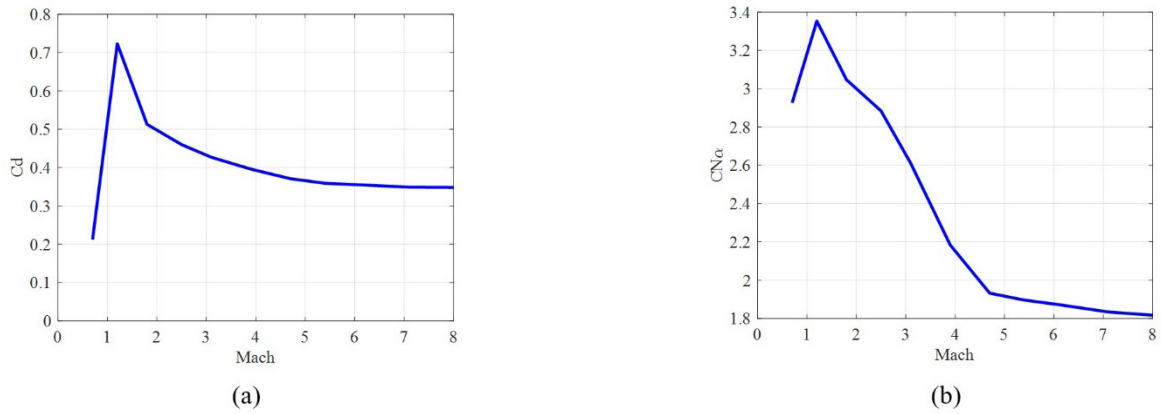


Figure 9 *Aerodynamic coefficients: (a) drag coefficient (b) slope of normal force coefficient*

4.2 Optimized trajectory

According to Motiwala et.al (2014), an optimized trajectory calculation is a key aspect in the design of an LV. In the present work, the trajectory was calculated using the Astos® (2011) software. The calculation method seeks the optimum point of an objective function, which consists of reaching the desired orbit, while maximizing efficiency and minimizing fuel consumption.

Figure 10 shows some parameters obtained for the optimized trajectory for the Micro-LV flight. The performance characteristics required for the satellite deployment mission were achieved. Figure 10 (a) shows the desired altitude of 300 (km). Figure 9(b) shows Δv1 of 2.04 (km/s) at 131 seconds, marking the end of the first stage burn, and Δv2 of 5.31 (km/s) with the final mission time of 943.7 seconds, resulting in a final velocity of 7.73 (km/s). Figure 10 (c), the final mass of 406 (kg) subtracted from structural mass of the second stage of 305.35 (kg), Table 2, it yields the payload mass

of 100.65 (kg), meeting the mission requirements. The Figure 10 (d) shows the longitudinal acceleration, whose values directly affect the calculations of sloshing frequencies, as previously shown in Equation 2.

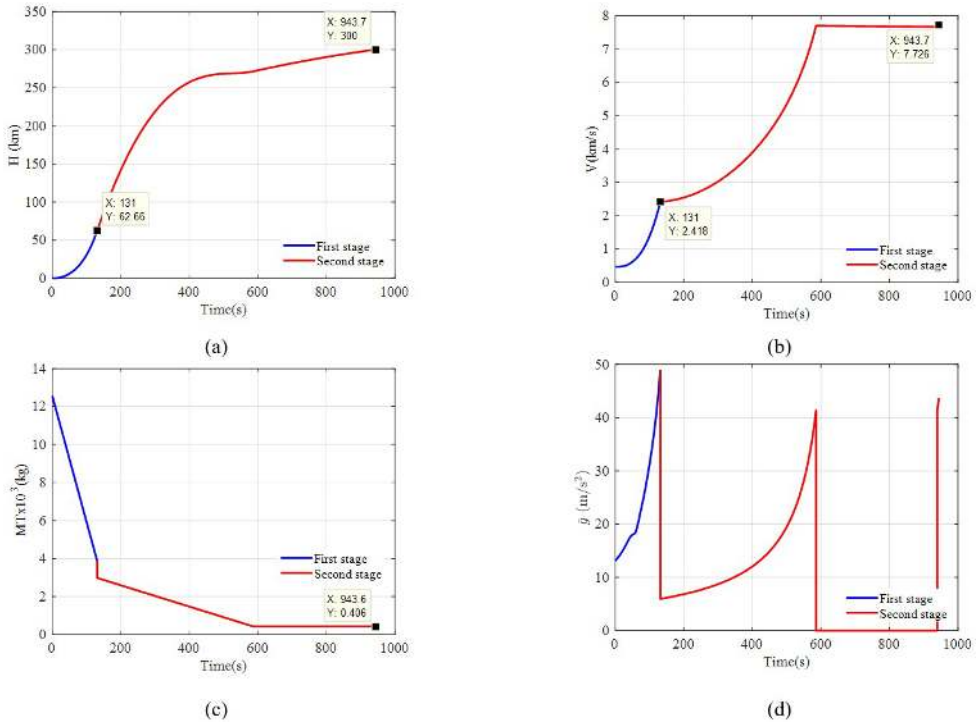


Figure 10 *Trajectory parameter: (a) altitude (b) inertial velocity (c) total mass (d) longitudinal acceleration*

4.3 Sloshing

Due to the consumption of propellant during the flight, the sloshing parameters for the LOX and RP-1 tanks were calculated for fill ratios range 0% ≤ FR ≤ 100%, in increments of 10%. As outlined in Section 2.1, the sloshing parameters depend on the zeros of the Bessel function, as indicated in Equation 2, which are related to the respective modes. For comparison purposes, the first five modes of vibration were considered.

Figures 11 (a) and 11 (b) show the sloshing masses curves of the for the LOX and RP-1 tanks, respectively. It can be observed that the sloshing mass values of the first mode are higher than those of the other modes. Therefore, the analyses presented here focus exclusively on the first mode of sloshing.

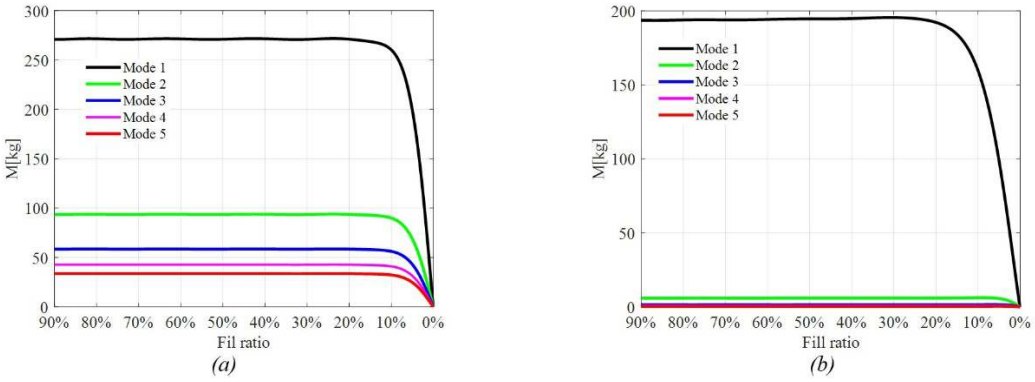


Figure 11 *Sloshing Parameters (a) Sloshing-LOX Mass (b) Sloshing Mass-RP-1*

The sloshing frequencies derived from Equation 12 are affected by the longitudinal acceleration of the Micro-LV. As can be seen, the sloshing frequencies values of LOX and RP-1 tanks, Figures 12 (a) and (b), respectively, are quite similar due to the equal diameters.

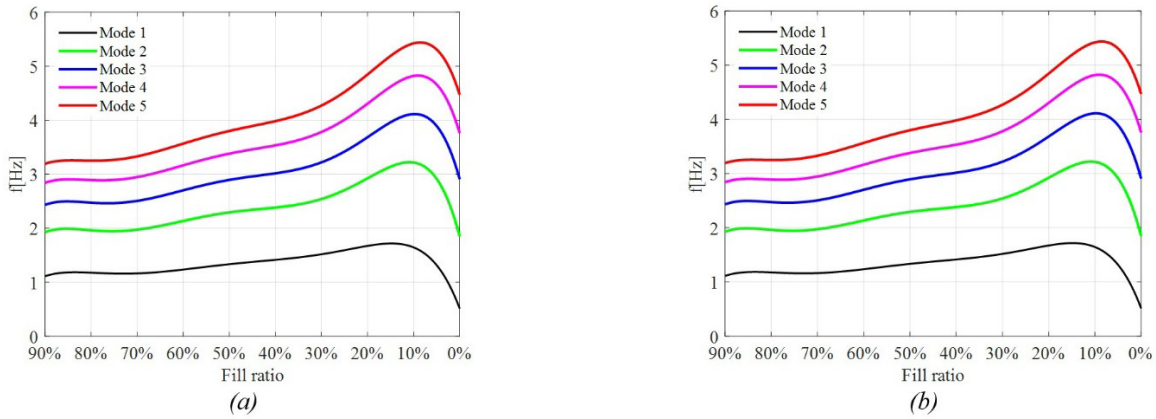


Figure 12 *Sloshing Parameters: (a) sloshing-LOX frequency (b) RP-1 sloshing frequence*

The position of the sloshing masses relative to CG of the LOX and RP-1 tanks were calculated using Equation 7. The values of the fixed masses and their respective positions were calculated according to Equations 8 and 9, respectively. Their positions were properly located within the Micro-LV model, as shown in Figure 8. These procedures were necessary for calculating the mass properties and moments of inertia of the Micro-LV for the finite element model (FEM).

4.4 Stability

The analysis focused solely on the flight of the first stage. Due to the proximity of the sloshing frequencies of the two tanks, the Bauer's analytical criterion (1967) may lead to inaccurate results, as noted by Barrows and Orr (2021). A Matlab® code (2018a) was developed to implement the state space formulation described in Section 2.3. The dynamic model transfer functions relating the pitch angle ϕ_y and engine angle β_{Ey} have been determined. Stability analyses with sloshing effects were performed in an open loop**,** considering a PD controller.

4.4.1 Danger zone

Figure 13 shows the positions of the sloshing masses for the LOX and RP-1 tanks along the length of the Micro-LV. It is noted that for the whole fill ratio range (0% ≤ FR ≤ 100%), only the sloshing mass of the RP-1 tank is located within the danger zone. Consequently, the analyses were performed only for this mass.

4.4.2 Controller Parameters

For attitude control, a PD controller was assumed. It was based on the Micro-LV rigid body data taking its aerodynamics into account. Table 3 below presents the gains considered for the fill ratio range of interest. The values of the gains were determined according to Equations 58 and 59, Section 2.4. A control frequency of ω_c=1.42 (Hz) defined as one-fifth of the lowest bending frequency (see Figure 17(b)), as outlined by Mooij and Gransden (2016) and damping of ζ_c = 0.805 were considered.

Table 3 Controller Parameters

Controller	Fill Ratio					
	40%	**50%**	**60%**	**70%**	**80%**	**90%**
K_p	9.47	10.53	11.54	12.11	12.45	12.90
k_D	1.83	2.03	2.24	2.40	2.50	2.59

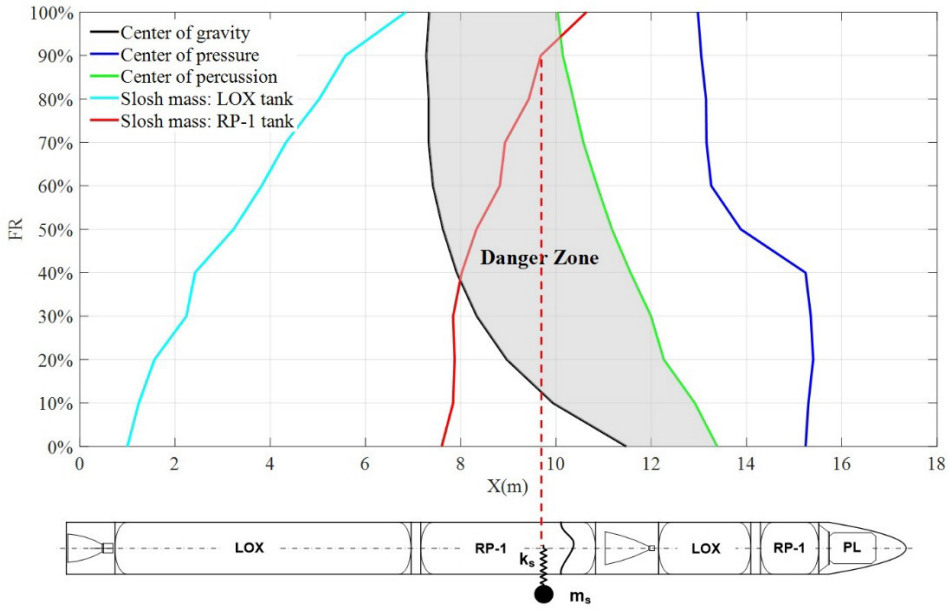


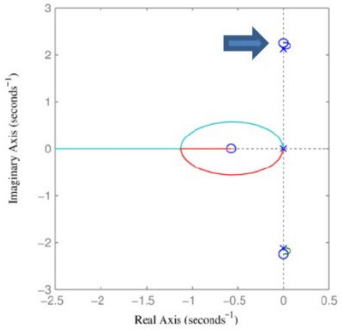
Figure 13 *Danger zone of the Micro-LV*

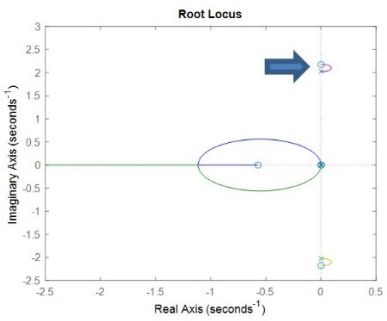
4.4.3 Verification calculations

Studies presented by Ottander et al. (2018) were used to validate the calculations performed by the code developed. In Figure 14, the expected root locus for the open-loop model of the Micro-LV is presented for ζ_s=0. The instability due to the sloshing effect can be observed on the imaginary axis. The angle of departure is directed toward the RHP, according to Pei (2021), Section 2.4.

Table 1. Example System Parameters

Name	Value	Units
$F(=R')$	$9x10^5$	N
M	$1.6x10^4$	kg
I	$9x10^5$	kg-m^2
$X_{c.g.}$	6	m
X_{s1}	9	m
m_{s1}	$1x10^3$	kg
ω_{s1}	2	rad/s
α_{s1}	0.1	1/m
a_0	0.08	rad/rad
a_1	0.14	rad/(rad/s)





(a) *(b)* *(c)*

Figure 14 *Verification Parameters: (a) LV data (b) original root locus (c) root locus reproduced*

4.4.4 Sloshing Effects Without Flexibility

In Figure 15, it can be observed that as FR increases, the frequencies (imaginary part) on the root locus, decrease, while the real part increases, tending to shift toward the RHP. This behavior indicates that with larger volume of propellant in the tanks, the instability due to sloshing effects becomes more imminent. This fact is evident upon reaching FR= 90%, as shown in Figures 15 (c) and (d), when the sloshing frequency associated with the open-loop transfer function zero becomes higher than its pole frequency, characterizing the sloshing instability.

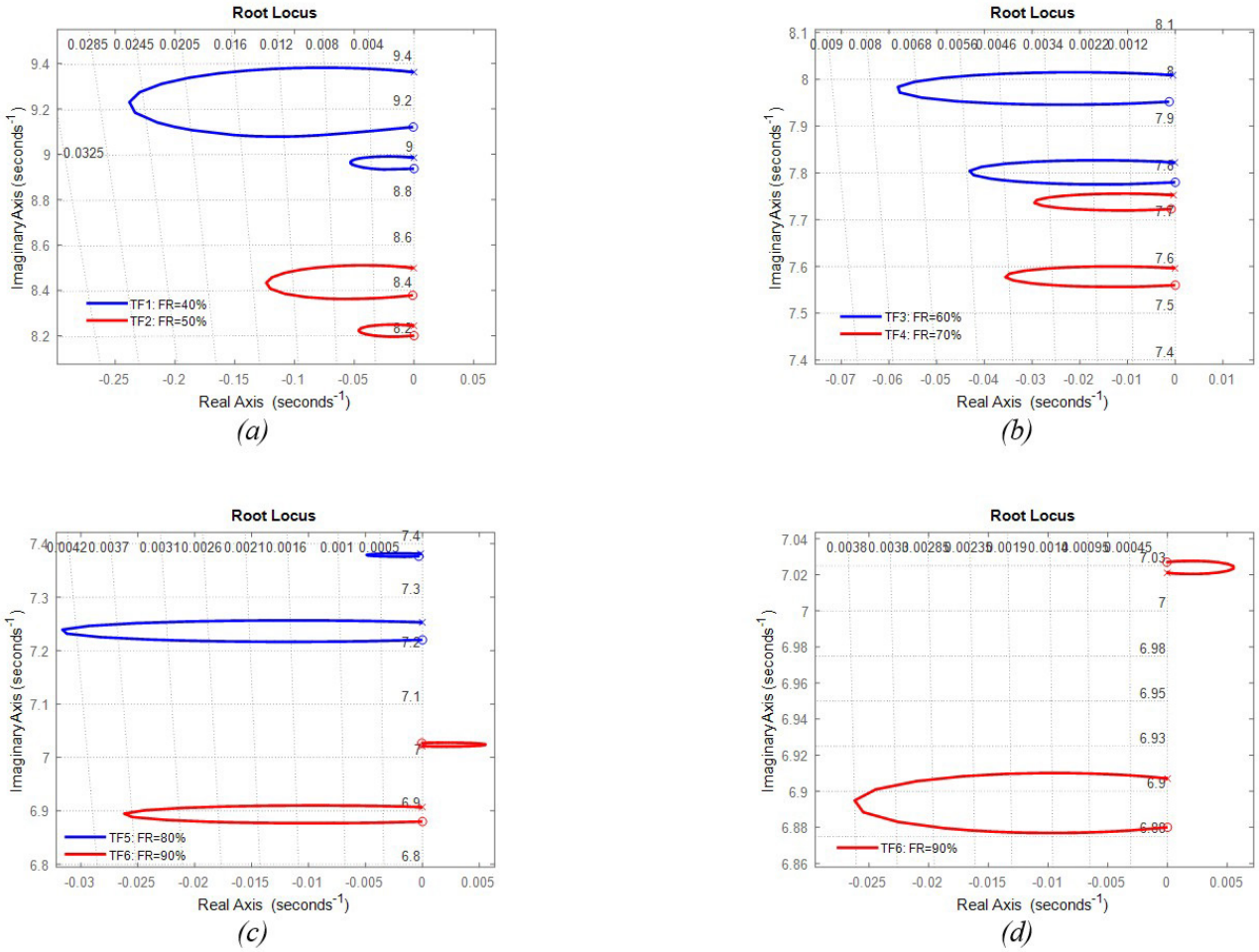


Figure 15 *Effects of sloshing without flexibility with ζ_s=0: (a) FR=40% and 50% (b) FR=60% and 70% (c) FR=80% and 90% (d) detail FR=90%*

4.4.5. Effects of Sloshing with Flexibility

The vehicle's flexibility was obtained by carrying out a structural analysis. Since the dynamic model is axisymmetric, the natural frequencies and corresponding modal shapes are uniform in the lateral directions. The Micro-LV is modeled with finite beam elements and concentrated parameters of masses and springs as shown in Figure 16.

The FEMAP Nx Nastran® (2014) software was employed to determine the eigenvalues and eigenvectors considering modal damping ζ_B = 0.05, calculated for the range 0% ≤ FR ≤ 100%. Figure 17 (a) shows the evolution of frequencies for 0% ≤ FR ≤ 100%. Figure 17 (b) shows the modal shapes of the first three bending modes for the condition of FR=90%, to be considered in the stability analysis.

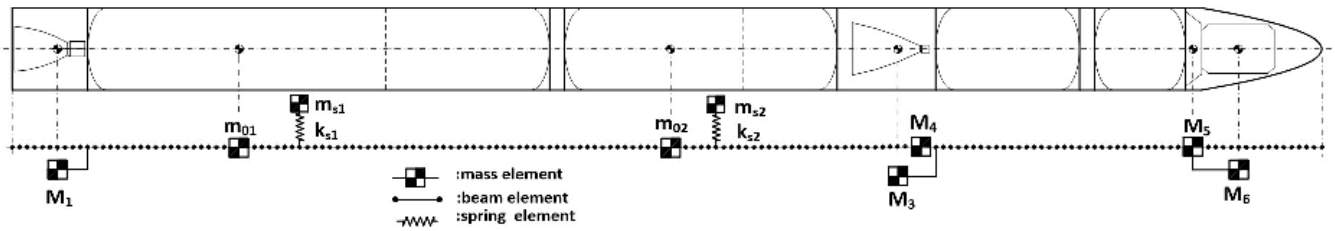


Figure 16 *Layout of the Micro-LV and the corresponding finite element model.*

Figure 18 shows the root locus for the first three bending modes of the Micro-LV. It is observed that the root locus is in the LHP with frequencies far from the imaginary axis indicating that the Micro-LV has adequate damping. Comparing the frequency value of the first bending mode, which is 6.75 (Hz) as seen in Figure 17(b), with the sloshing frequency of the RP-1 tank at 1.1 (Hz), Figure 12(b), we obtain a frequency band of 5.65 (Hz). Such a value avoids instabilities related to resonance.

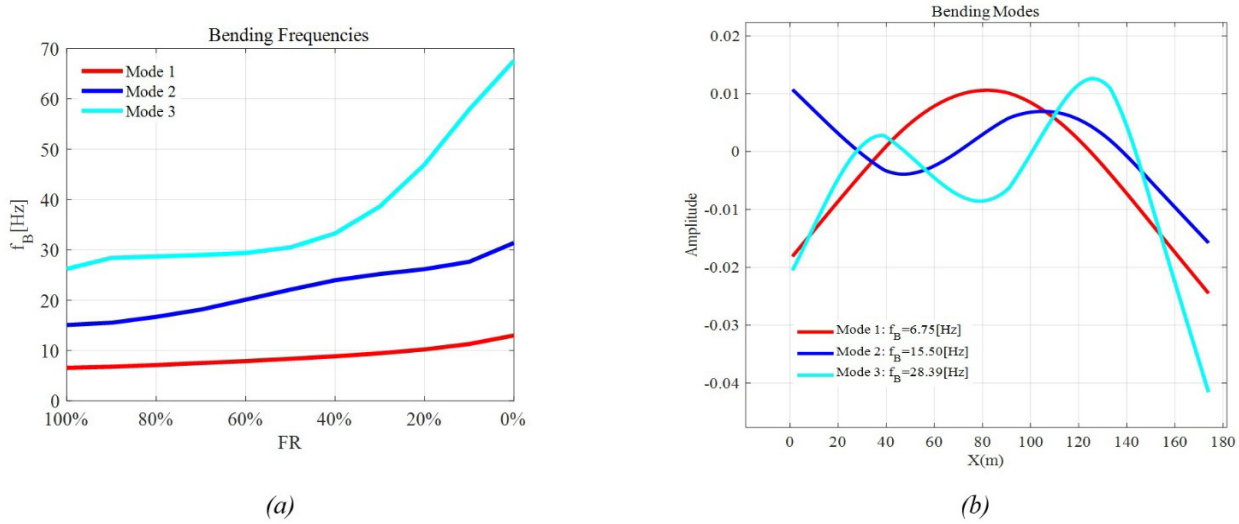


Figure 17 *Modal analysis (a) natural frequencies of the Micro-LV for 0% ≤ FR ≤ 100%. (b) bending modes of the Micro- LV for FR=90%.*

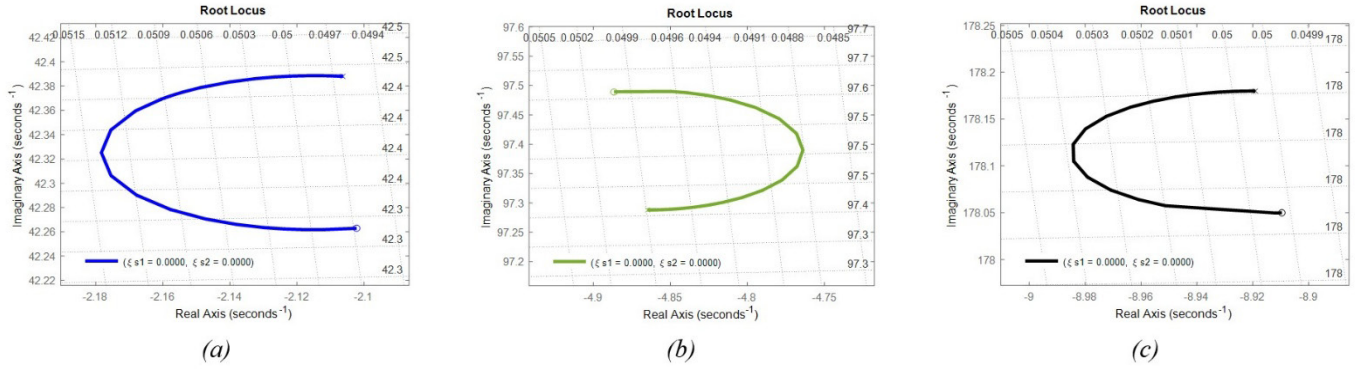


Figure 18 *Effects of sloshing on flexibly with ζ_s = 0 and FR=90%: (a) first bending mode (b) second bending mode (c) third bending mode.*

Figure 19 shows the root locus regions of the LOX and RP-1 tanks. For the LOX tank, Figure 19(a), the behavior is not affected by flexibility. Regarding the RP-1 tank, there is a slight tendency for the flexibility of the Micro-LV to damping the sloshing effect, but not significantly enough to mitigate the instability.

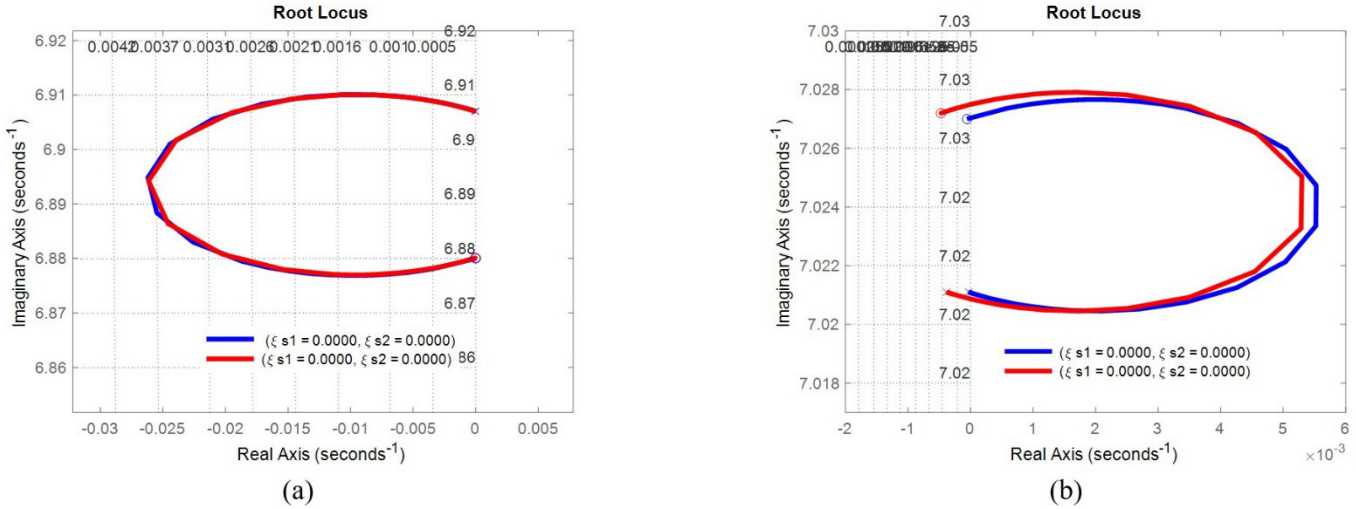


Figure 19 *Effects of flexible on sloshing with ζ_s = 0 and FR=90%: (a) LOX (b) RP-1*

4.4.6 Mitigating the effects of sloshing

The methods for mitigating the effects of sloshing can follow an active or passive approach. In the active form, additional elements are employed within the control system in the form of filters, with the advantage of not imposing any penalty in terms of weight. However, it is not always possible to synthesize such systems. Passive methods are safer, but they incur a weight penalty, as they are implemented through baffles introduced internally within the tanks, Ringland (1968).

Mitigating the sloshing effects is addressed in Section 2.1.2. For the analyses, the structural damping of the LV body was disregarded for the analysis, since flexibility did not show significant improvement in sloshing damping, as can be seen in Figure 18(b). Initially, viscous damping was considered with values of ζ_{s1} = 0.0002 and ζ_{s2} = 0.0007 for LOX and RP-1, respectively, according to Mooij and Gransden (2016). The minimum damping requirement can be determined by varying the values from ζ_{s2} = 0.0007, remaining ζ_{s1} = 0.0002 as a fixed value. The minimum damping value can be selected for regions where the root locus is entirely located in the LHP.

Figure 19(a), shows that the variations of ζ_{s2}, RP-1 tank, affect the root locus of the LOX tank, which evidences the sloshing coupling between the tanks. Figure 20(b) shows that from the value of ζ_{s2} = 0.0014, a minimum damping requirement can be established.

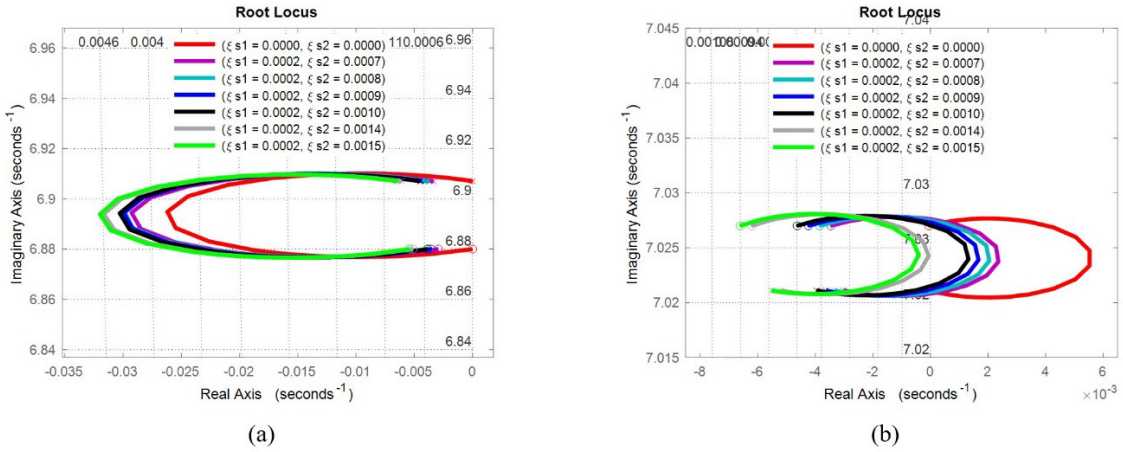


Figure 20 *Mitigation of sloshing effects through damping variation for FR=90% (a) LOX (b) RP-1*

For a preliminary design of the RP-1 tank ring baffles, the minimum damping requirement is considered with the value of ζ_{s2} = 0.0015, in order to cover any uncertainties. From Equation 15, we have that $\zeta_{s2} = \gamma$, and combining Equation 16 with a value of w = 0.025 (m), we determine a distance between the ring baffles of h_s = 0.357(m) with a total of 9 baffles, for the height of the tank with $H_{RP\text{-}1}$ = 3.6 (m), as shown in Figure 21. This figure shows the design scheme of the ring baffles along the entire length of the RP-1 tank. In this case, at least the first three upper rings can be considered, in order to cover the FR=90%.

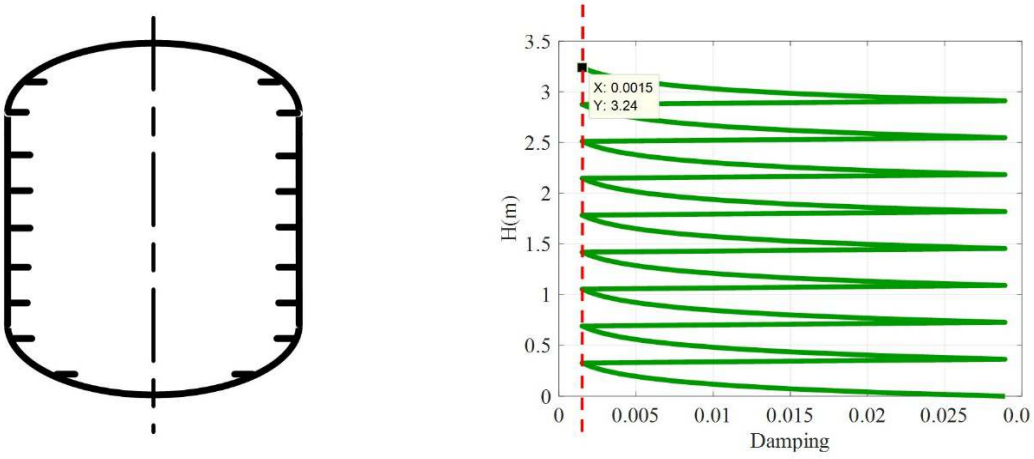


Figure 21 *Diagram of the design of the ring baffles: RP-1.*

5 REMARKS AND CONCLUSIONS

This paper presents a methodology for studying the effect of liquid propellant sloshing on the stability of a launch vehicle. The methodology allows one to identify the fill rates that lead to instability and to assess the amount of damping required to mitigate the unstable behavior. Then, it is possible to define the number of ring baffles (and its size) capable of introducing the necessary damping.

To carry out a case study it was necessary to face the lack of design data for this class of vehicles, for reasons of confidentiality. It was then decided to hold the preliminary design of a concept vehicle. The data from this project can be useful as a reference for future similar studies by other authors. The phase of the flight analyzed is in the initial part of the upward trajectory, when the launcher is subject to atmospheric disturbances and is propelled by the first stage.

Sloshing was included in the vehicle equations of the motion by means of equivalent mass-spring-damping mechanical models. Through root locus analyses performed with MATLAB routines, it was possible to verify that sloshing would generate instability only in the fuel tank and in the moment that the filling ratio of this tank is reduced to 90%. The point defined by the position of the tank sloshing mass of fuel and the fill ratio of 90% belongs to the danger zone for sloshing by Bauer's criterion. However, according to this criterion, several other fill ratios would lead to instability, which was not confirmed by the numerical models. This corroborates the limitation of Bauer's criterion for analyzing a launcher with two tanks.

It was possible to also verify the coupling between the dynamic behavior of the fuel and oxidizer tanks regarding sloshing, with the damping of one influencing the other. Additionally, it was observed that, in the studied case, the vehicle's flexibility acted slightly stabilizing in relation to sloshing. The relationship between the instability caused by sloshing in the vehicle dynamics and the propellant tank filling ratio was investigated, and the instability point was identified.

The methods for mitigating the effects of sloshing can follow an active or passive approach. In the active form, additional elements are employed within the control system in the form of filters, with the advantage of not imposing any penalty in terms of weight. However, it is not always possible to synthesize such systems. Passive methods are safer, but they incur a weight penalty, as they are implemented through baffles introduced internally within the tanks. In the present work, the use of ring baffles was proposed as solution to mitigate the unstable behavior. Finally, the number of necessary rings and their dimensions were defined.

A possible future work is to study the flight of the second stage and comparing the sloshing effect with filtering techniques, to allow decision-making in the design development phases, since the dampers can penalize the satellization mass.

Acknowledgments

This study was financed in part by the Coordenação de Aperfeiçoamento de Pessoal de Nível Superior - Brasil (CAPES). Finance Code 001.

The authors would like to acknowledge the support provided by CAPES for this work.

Author's Contributions: Conceptualization, DS Aguiar, C Souto and M silva; Methodology, DS Aguiar and G Silveira; Software, DS Aguiar and G Silveira; Investigation, DS Aguiar and G Silveira; Writing - original draft, DS Aguiar and C Souto; Writing - review & editing, D Aguiar, C Souto and M silva; Funding acquisition, C Souto and M silva; Supervision, C Souto and M silva.

Data availability: Research data is available in the body of the article

Editor: Pablo Andrés Muñoz Rojas

References

Abramson, H., N. (1966). The Dynamic Behavior of Liquids in Moving Containers. NASA SP – 106.

Astra Rocket 4(2020). Payload User’s Guide.

Barrows T. and Orr J. (2021). Dynamics and Simulation of Flexible Rockets. Elsevier Academic Books.

Bauer, B. F. (1967). Stability Boundaries of Liquid-Propelled Space Vehicles with Sloshing," Journal of Spacecraft, Vol. 1, No. 7, pp. 1583–1589.

Bijelde, B., Vozoff, G., and Shotwell, G. The Falcon 1 Launch Vehicle: Demonstration Flights, Status, Manifest and Upgrade Path. SSC-07-III-6, 21st Annual AIAA/USU Conference on Small Satellites, 2007.

Blake, W.B. (1998), "Missile datcom: user's manual-1997FORTRAN 90 revisions", Air Force Research Lab Wright-

Craig, R., R., Jr. and Kurdila., J. a. (2006). Fundamentals of structural dynamics 2nd ed, 2006 by John Wiley & Sons. Inc.

Dodge, F., T. (2000). The New Dynamic Behavior of Liquids in Moving Containers. Southwest Research Institute. (SRI).

Edberg, D. and Costa W. (2022). Design of Rockets and Space Launch Vehicles, Second edition, 2022 AIAA.

Electron (2022). Payload User's Guide. Nov.

Falangas E., T. (2016). Performance Evaluation and Design of Flight Vehicle Control System. IEEE Press.

Falcon1 (2008). Launch Vehicle Payload User's Guide. Spacex. Rev.7.

FEMAP Nx Nastran. (2014). "Educational License".

Firefly Alpha (2016) Payload User's Guide Version 1.2.

Garner, D. (1964). Control Theory Handbook, Tech. Rep. TM X-53036, NASA.

Greensite A., L. (1970). Analysis and Design of Space Vehicle Flight Control Systems. Spartan Books, New York.

Greensite, A. L., Analysis and Design of Space Vehicle Flight Control Systems, Volume VII - Attitude Control During Launch, NASA TM, Washington D.C., 1967.

Ibrahim, R., A. (2005). Liquid Sloshing Dynamics - Theory and Applications. Cambridge University Press

Jang, J., W., Alaniz A. and Yang L. (2013). Mechanical Slosh Models for Rocket-Propelled Spacecraft. American Institute of Aeronautics and Astronautics AIAA 2013-4651.

Kulu, E. (2021)., Small Launchers. (2021). Industry Survey and Market Analysis. 72nd International Astronautical Congress (IAC 2021), Dubai, United Arab Emirates, 25-29 October 2021.Copyright © 2021 by Erik Kulu. Published by the IAF, with permission and released to the IAF to publish in all forms.

Miles, J. W. (1958). Ring Damping of Free Surface Oscillations in a Circular Tank, ASME J. Applied Mechanics, 25, pp. 274-276.

Mooij, E. and Gransden, D., I. (2016). The Impact of Aeroelastic Effects on the Controllability of Conventional Launch Vehicles. 67th International Aeronautical Congress, Guadalajara, México. IAC-16-C2.3.12x35230.

Motiwala S.A., Mathias, D., L. and Mattenberger, C., J. (2014). Conceptual Launch Vehicle and Spacecraft Design for Risk Assessment". NASA/TM-2014-218366.

Nichawde, C., Harish, P.M., Ananthkrishnan, N. (2004). Stability analysis of a multibody system model for coupled slosh–vehicle dynamics Journal of Sound and Vibration 275 1069–1083.

Ottander, J., A. Hally, R., A. and Powers J. F. (2018). Practical Methodology for the Inclusion of Nonlinear Slosh Damping in the Stability Analysis of Liquid-propelled Space Vehicles.

Pei, J. (2021). Analytical Investigation of Propellant Slosh Stability Boundary on a Space Vehicle.

Pelton J. N. and Laufer R. (2019). Commercial Small Satellites for Business Constellations Including Microsatellites and Minisatellites. Springer Nature Switzerland AG 2019 J. Pelton (ed.), Handbook of Small Satellites.

Ringland, R.F. (1968). Dynamic Stability of Space Vehicles Volume X – Exit Stability. NASA CR 935. General Dynamics Corporation. San Diego California. USA.

Schlingloff, H. (2005). "Astronautical Engineering – An introduction to the Technology of Spaceflight" Bad Abbach, Germany.

Shekhawat, A., Nichkawde, C., Ananthkrishnan, N. (2006). Modeling and Stability Analysis of Coupled Slosh-Vehicle Dynamics in Planar Atmospheric Flight. 44th AIAA Aerospace Sciences Meeting and Exhibit 9 - 12 January 2006, Reno, Nevada. AIAA -427.

Sutton, G., P and Blibarrz, O. (2010). Rocket Propulsion Elements, 8th Edition, John Wiley & Sons, New York.

MATLAB (R2018a). The MathWorks, Inc. (2018). [Software]. https://www.mathworks.com/

Wekerle, T., Pessoa F, J.B.; Costa, L. E.V. L. and Trabasso, L.G. (2017). Status and Trends of Smallest's and their Launch Vehicles — An up-to-date Review. J. Aerosp. Technol. Manag. São José dos Campos, Vol.7, No 3, pp.269-286, jul.-Sep., 2017.

Xin, T., Duan, Y., Zhang S., Cui C. and Bai G. (2018). An Equivalent Propellant Sloshing Model of Ellipsoid Cylindrical Tank. 2018 2nd International Conference on Systems, Computing, and Applications (SYSTCA 2018).

Zhuang, L. and Yulin Z. (2021). Deformation Reconstruction and High-Precision Attitude Control of a Launch Vehicle Based on Strain Measurements. Hindawi International Journal of Aerospace Engineering Volume 2021, Article ID 6672943, 20 pages.